Dear Editor,

We would like to submit our revised manuscript entitled "**Seasonal changes in sea ice kinematics and deformation in the Pacific Sector of the Arctic Ocean in 2018/19**" [Paper # tc-2020-211] , which is submitted for possible publication in the the Cryosphere. According to the comments from anonymous reviewers and you, we made a major revision of the manuscript by carrying out the following tasks:

1) We restructured the manuscript, especially for the sectors of Introduction, Discussion, and Conclusions, to make it more compact and focusing.
2) In terms of methodology, we improved it to make the expression clearer and added some sensitivity calculation. In particular, we have added an explanation of how to distinguish contributions from inertial and tidal oscillations to sea ice kinematics.
3) We enhanced the comparison with the results from other studies.
4) We checked the language through the manuscript, revised some figures, and made the expressions clearer.
5) We added some discussions on the implications of enhanced ice deformation on the biological processes.

Please find the following files in our submission package:
1) The manuscripts with tracked changes,
and 2) Response letter.

Thank you for your time.
Sincerely,
Ruibo Lei, other co-authors

Reply to reviewer 1

1 It is not clear from the conclusions, abstract and results where the emphasis is in this paper, with too much attention paid on the synoptic conditions over the key finding. I think the key point is that the space-time coupling for ice deformation changes over the transition from free drift to a consolidated ice pack. This point is worth reporting, as I believe it has not been shown with clarity before. However there are some points to address to make sure that this result is real.

We restructured the sectors of abstract, introductions, and conclusions, and made them more focusing on the seasonal and spatial changes in sea ice kinematics and deformation, as well as their coupling. In terms of methodology, we improved it to make the expression clearer and added some sensitivity calculation. For example, we have added an explanation of how to distinguish contributions from inertial and tidal oscillations to sea ice motion (Lines 207-230, the line number refer to the revised manuscript with track changes); to test the sensitivity of the estimation of β to the number of samples, we also calculate the length scaling law using seasonal temporal window (Lines 494-498); to estimate the localization of ice deformation, we further use other thresholds to calculate the fractional areas accommodating the largest the ice deformation (Lines 529-534).

2 The study also shows a gradient in response to wind forcing across the Canada Basin that might be attributed to the different ice ages. It is shown that there is increasing localization of deformation as the ice pack become more consolidated, which is echoing work by Stern and Lindsay (2009).

We further compared our results with Stern and Lindsay (2009) (Lines 111-113; 492-494; 527), and highlight the spatial gradient of ice kinematics and ice deformation in response to wind forcing.

3 If you just consider the amplitude of semi-diurnal peak in the velocity you are mixing measurement noise and background energy cascade (typically red noise for ice drift) with the inertial motion. How can you be sure that you are actually not aliasing the inertial power due to weather changes? Are you really sure the peak is apparent for all months? You need to consider how high above the background the inertial peak sits. In some parts of the Arctic this peaks is tidal as well as inertial. You should comment on the roll of tides in the study region.

Inertial oscillations are clockwise oscillations in the northern hemisphere, in contrast to tidal oscillation, which can rotate clockwise or counter-clockwise (Gimbert et al., 2012).

Amplitudes shown in the original Figure 9 are that at the local maximum of negative inertial frequency (about -2.01 ~ -1.94 cycles per day) after complex Fourier transformation of monthly time series of normalized ice velocity. At this frequency, there is energy caused by inertial and tidal forcing and high-frequent components of wind and current forcing. In the revision, we also identify and show the amplitudes at the positive tidal frequency (+2 cycles per day) in the current Figure 9, which includes the energy from tidal forcing and background noise of high-frequent components of wind and current forcing. From the amplitudes at the positive tidal frequency, we cannot identify the obvious seasonal and spatial variations because all the buoys were deployed over the deep waters and the tidal forcing is relatively weak. In addition, both tidal forcing and high-frequent parts of wind and current forcing are not expected to have seasonal changes. Thus, the spatiotemporal change patterns of the amplitudes at negative inertial frequency are majorly attributed to the changes caused by inertial oscillations. We have added an explanation of how to distinguish contributions from inertial and tidal oscillations to sea ice motion (Lines 207-230; Line 371-391).

3. Can you comment on how accurately you can estimate the area localization, delta_15%, given the sparse nature of the buoy array? Is the trend in figure 14 statistically significant?
To estimate the area fraction of 15% largest ice deformation, we use the data obtained from the relatively dense buoy array deployed in the north of Pacific sector of Arctic Ocean, but not from all buoys (Line 260). We test the reliability for using the area fraction of 15% to estimate the area localization through using various fractions. (Lines 529-534)
The trend in Fig. 14 is statically significant at 0.001 level (Line 513).

4 Regarding the results, some are not consistent with previous studies. However there is insufficient information in the manuscript to identify if the results are reasonable based on the data. Your beta values, the spatial scaling exponent, are somewhat higher than values found in previous studies. I am referring to figure 12.
The spatial scaling exponent is strongly dependent on the ice cohesiveness and temporal sampling rate. In the Fig. 12, the results include the results obtained from September and at the 1-h temporal resolution, thus including some relatively large values. The value obtained in Jan-Feb. with the 3-h temporal resolution was 0.42–0.44, which was comparable with that obtained in Beaufort Sea during March-May 2007 (0.40) (Itkin et al., 2017). As our known, Arctic sea ice in the Pacific Sector may reach to its annual maximum thickness in May or early Jun. (e.g., Perovich et al., 2003). The strongest ice cohesiveness would occur during the latter winter or early spring. This is because, in the mid-winter, the ice thickness still doesn't reach the annual maximum although the air temperature is coldest. In the revision, we enhanced the comparison with the results from other studies. (Lines 486-494)

5 A similar decrease in beta with sampling interval, the space-time coupling, was found by Hutchings et al. 2018, who only had data for March through May. It is interesting that you find c (the gradient in log space) increases from a time the pack is in free drift to a time it is more consolidated pack. I have one suggestion to make sure your results are robust: Is there sufficient data to identify beta in only one month? I have looked at this myself and find the results to be quite messy when I split time series of buoys array deformation by month.
As mentioned above, we highlighted the new findings for the space-time coupling of

ice deformation.
To estimate the beta, we use the strain rate obtained from all triangles consisting of any three buoys, which can guarantee the magnitude of statistical samples. This method is a little different from that given by Hutchings et al. (2018), who estimated the deformation rate using the fixed buoy-triangle groups, and has been used by Itkin et al. (2017), who also estimate the beta using the data obtained from one month. (Line 218)
To test if our results are robust, we also estimate the seasonal beta, i.e., those obtained in autumn (September-November) and winter (December-February). (Lines 495-498)

6 Incidentally there are many places in the paper where the language is implying something causes the other, such as more consolidated ice pack causes lower beta and higher c. I would suggest you consider that patterns that covary do not indicate they cause one another, but perhaps they could be related. Consider being careful you're your language throughout.
Thanks for the suggestions. We checked the language through the manuscript and made sure that the expression is rigorous and clear.

7 The paper could be refocused in the abstract, discussion and conclusion to focus attention on the main findings. While the synoptic situation is important and it needs to be mentioned how the ice pack responded dynamically to seasonal synoptic changes, these details distract from the main points.
Thanks for the suggestions. In the revision, we focus on the seasonal changes in the ice deformation and its space-time coupling. We restructured the sectors of abstract, introductions, and conclusions, and made them more compact and focusing.

8 line 21: It is not clear what "Areal localization index" is in the abstract. Perhaps use plain language here rather than jargon.
We used the plain language in the abstract. (Lines 22-23)

9 Please check for small grammatical errors. For example line 28 in the abstract "ore pronounced in the future as sea ice losses at higher rates in the". I think "as ... " should be "as sea ice losses are at higher ..."
We checked the grammatical errors through the manuscript.

10 line 43: The first sentence is hanging here, I think you need to clarify what you mean by deformation.
We corrected this mistake in expression (Lines 44-45).

11 line 68/69: "inertial signal". You need a better description of the inertial oscillation of the ice-ocean boundary layer in response to impulses imparted by sudden changes in wind direction.
We added the discussions on the inertial oscillation of the ice-ocean boundary layer in response to impulses imparted by sudden changes in wind direction. (Lines 81-83;

368-371)

12 line 108, using semi-colons will help separate items in the list. line 116: "From" should be "Of" line 129: remove "have"
We corrected these mistakes in expression. (Lines 130-137; Line 141)

13 line 136: I do not understand what you are calculating over the buoys that are 1 standard deviation from mean latitude or longitude. Why choose one standard deviation? This seams arbitrary and whether there are distortion effects related to the spherical coordinates depends on the array size, and 1 standard deviation probably changes over the time the buoy array exists.
We gave details on the changes in the geographical distance according to our use of 1 standard deviation of latitude and longitude; and added some discussions on the reliability of this treatment method. (Lines 164-171)

14 line 156: "Because of the delayed release of NSIDC data ..". I suspect you might be able to get more recent data if you ask Mark Tshudi personally.
We are using the latest version of the data, which is updated by December 2018 (Version 4; Tschudi et al., 2019 and 2020). Because this is just the supporting data, we consider that the lack of some comparative data will not have a significant impact on our results.

15 Regarding the inertial motion index. How do you ensure this is actually a peak and not background noise?
In fact, the peak value of inertial oscillation might be affected by the high frequency variations of wind or current, but the influence is very small. We selected the peak value manually in the range of ±0.03 cycles per days from the targeted frequency. In the reversion, we further explained the method. When the inertial oscillation is very weak (with ~15% cases), we use the amplitudes at $-f_0$ as the IMI, which actually is background noise, but also can indicate a state with an almost negligible inertial oscillation occurred only in winter. Therefore, these conditions will not affect our identification of the seasonal variation of the contribution of the inertial oscillation on ice motion. (Lines 207-230)

16 equations 6 and 7: I think you need to specify that beta and alpha are the scaling exponents for the mean deformation. As sea ice deformation is multifractal, the exponents vary for the different moments of the deformation distribution.
We specified that beta and alpha are the scaling exponents for the mean deformation. (Lines 323-325)

17 line 209, this sentence is a little clunky. I think you want to say you calculate the empirical orthogonal functions for the sea level pressure. Also, did you expand SLP earlier?
Yes, we calculate the empirical orthogonal functions for the sea level pressure. We

made the expression clearer (Line 345-346). We have expanded SLP already in Line 235.

18 line 498-490, and line 28-29: This seems to be conjecture. The ice in this region is already mostly seasonally any way so I think it is moot point that there will be further losses in these regions.
Yes, the ice in these regions is already mostly seasonally in the west and south parts for PAO. However, the further lengthened ice melt season, and the increased length of free-ice waters occupation, will shorten the growth season of sea ice and reduce the ice thickness, thus enhancing the response of sea ice kinematics and dynamic deformation to atmospheric forcing. We added some discussions on this feedback regime. (Lines 755-769)

19 Finally some of the figures are overly cramped in their use of space. e.g. figure 9 almost has labels for sub panels overlapping. The month lables are hidden inside the figures and a little bit of space below the color bar would help readability. Figures 10, 15 have similar issues.
We improved these figures.

Reply to reviewer 2
1 Tide is an important contributor to sea ice deformation. Thus, the discussion about the effects of tide is of interest to improve the understanding of this study.
Yes, tide is an important contributor to sea ice deformation, especially over the shallow waters. However, using the buoys data, it is hard to identify the effect of tide forcing on ice deformation directly.
In the revised manuscript, we added some quantitative discussions on the effect of tidal forcing on ice motion (Lines 295-298; 534-537). Compared with the inertial oscillation, the contribution of tidal oscillation is relatively weak, which gives a negligible contribution to the seasonal and spatial changes on the quasi-semidiurnal oscillation of ice motion. From this analysis, we infer that the influence of tidal forcing on ice deformation also is negligible regardless of seasons (Lines 534-537).

2 The results of this study are insightful. However, to make the results more robust, some comparisons between results of this study and those of other regions or satellite observations are encouraging.
Thanks for the suggestions. To enhance the representativeness of our results and give some basin-scale implications for the ice dynamics, we added some comparisons with results obtained from close regions, as well as that obtained from the estimations based on satellite observations. (Lines 688-696; 714-721; 734-738)

3 Arctic sea ice decline is in a faster track and the ecological impacts are more apparent. Therefore, it would be useful to discuss the association between sea ice deformation and Arctic sea ice decreases and related ecological process.

We added some discussions on the implications of enhanced ice deformation on some ice-associated ecological processes. (Lines 939-951); and the association between Arctic sea ice deformation and sea ice decrease (Lines 755-769).

4 L29, “western parts” -> “eastern parts”? L97 “for example” -> “, for example,” L116 “From” -> “of”

We corrected these linguistic errors, and checked the language through the manuscript again.

5 L37, “enhanced Arctic Dipole (Lei et al., 2016)-> some other references may be relevant, such as:

Bi, H., Yang, Q., Liang, X., Zhang, L., Wang, Y., Liang, Y., and Huang, H., 2019, Contributionsof advection and melting processes to the decline in sea ice in the Pacific sector of the Arctic Ocean. The Cryosphere, 13, 1423-1439.

Ding, Q., et al., 2017, Influence of high-latitude atmospheric circulation changes on summertime Arctic sea ice. Nature Climate Change, 7, 289-295.

We cited these two references and enhanced the discussions on the influence of atmospheric circulation on ice motion (Lines 87-91; 368).

6 Figures 9 and 10 need rearrangement to make it clearer.

We improved these figures.

Seasonal changes in sea ice kinematics and deformation in the Pacific Sector of the Arctic Ocean in 2018/19

Ruibo Lei[1], Mario Hoppmann[2], Bin Cheng[3], Guangyu Zuo[1,4], Dawei Gui[1,5], Qiongqiong Cai[6], H. Jakob Belter[2], Wangxiao Yang[4]

[1] Key Laboratory for Polar Science of the MNR, Polar Research Institute of China, Shanghai, China.

[2]Alfred-Wegener-Institut Helmholtz-Zentrum für Polar- und Meeresforschung, Bremerhaven, Germany.

[3] Finnish Meteorological Institute, Helsinki, Finland.

[4] College of Electrical and Power Engineering, Taiyuan University of Technology, Taiyuan, China.

[5] Chinese Antarctic Center of Surveying and Mapping, Wuhan University, Wuhan, China.

[6] National Marine Environmental Forecasting Center of the MNR, Beijing, China.

Correspondence to: Ruibo Lei (leiruibo@pric.org.cn)

Abstract. Arctic sea ice kinematics and deformation play significant roles in heat and momentum exchange between atmosphere and ocean, and they have a profound impact on biological processes and biogeochemical cycles. However, mechanisms regulating their changes at seasonal scales remain poorly understood. Using position data of 32 buoys in the Pacific sector of the Arctic Ocean (PAO), we characterized spatiotemporal variations in ice kinematics and deformation for autumn–winter 2018/19 over the transition from melting ice to a near consolidated ice pack. In autumn, the response of sea ice drift ~~response~~ to wind forcing and its inertial oscillation –were stronger in the southern and western than in the northern and eastern parts of the PAO. These spatial heterogeneities decreased gradually from autumn to winter, in line with the ~~seasonal evolution~~increases in ~~of~~ ice concentration and thickness. Correspondingly, ice deformation becomes much more localized as the sea ice mechanical strength increases, with the area proportion occupied by the strongest ice deformation ~~Areal localization index~~ decreas~~ed~~ing by about 50 % from autumn to winter~~, suggesting the enhanced localization of ice deformation as the increased ice mechanical strength~~. ~~In winter 2018/19, a highly positive Arctic Dipole and a weakened high pressure system over the Beaufort Sea led to a distinct change in ice drift direction and an temporary increase in ice deformation.~~ During the freezing season, ice deformation rate in the northern part of the PAO was about 2.5 times that in the western part probably related to~~due to~~ the higher

spatial heterogeneity of oceanic and atmospheric forcing in the north. North–south and east–west gradients in sea ice kinematics and deformation of the PAO, as observed in this study~~autumn 2018~~, are likely to become more pronounced in the future as a result of a longer melt season, especially ~~sea ice losses at higher rates~~ in the western and southern~~ than in the northern and western ~~ parts.

1 Introduction

The Pacific sector of Arctic Ocean (PAO) includes the Beaufort, Chukchi, and East Siberian Seas, as well as the Canadian and Makarov Basins. Among all the sectors of the Arctic Ocean, decreases in both summer sea ice (Comiso et al., 2017) and multi-year sea ice (MYI) (Serreze and Meier, 2018) are the largest in the PAO in recent decades, and are most likely linked to enhanced ice–albedo feedback (Steele and Dickinson, 2016), increased Pacific water inflow (Woodgate et al., 2012), and enhanced Arctic Dipole (Lei et al., 2016). In the PAO, MYI is mainly distributed north of the Canadian Arctic Archipelago (Lindell and Long, 2016), suggesting a strong east–west gradient in sea ice thickness and strength. In summer, the marginal ice zone (MIZ), defined as the area where sea ice concentration is less than 80 %, can reach as far north as 80° N (Strong and Rigor, 2013), thus the south–north gradient in ice conditions in the PAO is expected to be greater than that in other sectors of the Arctic Ocean.

Sea ice deformation results from divergence, convergence, and shear~~ of ice floes~~, which can enhance redistribution of ice thickness through the formation of leads and ridges (Hutchings and Hibler, 2008; Itkin et al., 2018). Loss of MYI and decreased thickness weakens the Arctic sea ice cover, increases floe mobility (Spreen et al., 2011), and promotes ice deformation (Kwok, 2006)~~, which further enhances redistribution of ice thickness by producing leads and ridges (Itkin et al., 2018)~~. Leads forming between ice floes increase heat transfer ~~loss~~ from the ~~ice-covered~~ ocean to the atmosphere, a~~. This~~ process that is particularly important in winter because of the large temperature gradient (Alam and Curry, 1998)~~, and contributes considerably to the Arctic Amplification (Lüpkes et al., 2008)~~. In summer, cracks, leads or polynyas within ~~cCracks or leads in~~ the pack ice serve as windows that expose the ocean to more sunlight, which significantly alters biological processes and biogeochemical cycles such as promoting under-ice haptophyte algae blooms (Assmy et al., 2017). Under converging conditions, ice blocks are packed randomly during the formation of sea ice pressure ridges, creating water-filled voids that act as thermal buffers for subsequent ice growth (Salganik et al., 2020). The high porosity of pressure ridges creates~~results in~~ an abundance of nutrients for ice algae communities. As a result, pressure ridges can become biological hotspots (Fernández-Méndez et al., 2018). Thus, characterizations of sea ice deformation are not only relevant for a better understanding of ice dynamics and their roles in Arctic climate current change~~s in Arctic climate system~~, but especially ~~and~~ also of ice-associated ecosystems.

In the PAO, the generally anticyclonic Beaufort Gyre (BG) generates sea ice motion that is clockwise on average. The boundary and strength of the BG are mainly regulated by the Beaufort High (BH) (Proshutinsky et al., 2009; Lei et al., 2019). An a~~A~~nomalously low BH can result in a reversal of wind and ice motion in the PAO that is normally anticyclonic (Moore et al., 2018). Under a positive Arctic Dipole Anomaly (DA), more sea ice from the PAO is transported to the Atlantic sector of the Arctic Ocean (AAO), i.e., promoting ice advection from the BG system to the Transpolar Drift Stream (TDS) (Wang et al., 2009). In summer, such a regime would stimulate the ice–albedo feedback and accelerate sea ice retreat (Lei et al., 2016). The loss of summer sea ice in the PAO during the recent four decades can be explained using the increased ice advection from the PAO to the AAO by 9.6% (Bi et al., 2019). In the zonal direction, the enhanced anticyclonic circulation in the PAO can result in more ice advection from the Beaufort and Chukchi seas to the East Siberian Sea (Ding et al., 2017). The r~~R~~esponse of sea ice advection in this region to interannual variation of atmospheric circulation patterns has been studied extensively (e.g., Vihma et al., 2012), but investigations on a seasonal scale are relatively scarce.

From a dynamical perspective, sea ice consolidation has been ~~quantified~~ related to~~using~~ the strength of the inertial signal of sea ice motion (Gimbert et al., 2012), Ice–Wind Speed Ratio (IWSR) (Haller et al., 2014), localization, intermittence and space–time coupling of sea ice deformation (Marsan et al., 2004), as well as to the response of ice deformation to wind forcing (Haller et al., 2014). The inertial oscillation is caused by the earth's rotation and is stimulated by sudden changes in external forces, majorly due to enhanced wind stress on the ice-ocean mixing layer caused by storms/cyclones or moving fronts of extreme weather events~~because of storms or moving fronts~~ (e.g., Lammert et al., 2009; Gimbert et al., 2012). It ~~would~~is ~~be~~ weakened due to surface friction and internal ice stresses. The localization and intermittence of sea ice deformation indicate the degree of constraint for ~~the~~ its spatial range and temporal duration~~ of sea ice deformation~~ (Rampal et al., 2008). Space-time coupling demonstrates the temporal or spatial dependence for the spatial or temporal scaling laws of ice deformation, which can indicate the brittle behaviour of sea ice deformation (Rampal et al., 2008; Marsan and Weiss, 2010).

The inertial oscillations of Arctic sea ice motion (Gimbert et al., 2012) and the IWSR (Spreen et al., 2011) have been increasingly ~~demonstrated to increase as a result of~~associated with reduced sea ice thickness and concentration. However, the spatial variability of~~spatial difference in the effects of~~ sea ice consolidation~~ on its~~, kinematics and deformation on ~~synoptic and~~ seasonal scales in the PAO, where sea ice condition has strong spatial heterogeneity as mentioned above, remain unclear.

The application of drifting buoys to determine the properties and seasonal cycle of the atmosphere, ocean and sea ice on a basin scale and year-round has been an emerging field in polar research in recent years. For example, drifting buoys are a good tool to track relative ice motion. However, b~~B~~ecause of the usually limited number of such buoys deployed in any given ~~season~~ region and season due to cost and logistical limitations~~was limited~~, it has so far been difficult to accurately distinguish spatial variability and temporal change in sea ice kinematics and deformation from existing buoy data in the PAO. During spring 2003, the deformation of a single lead in the Beaufort Sea was investigated using Global Positioning System (GPS) receivers (Hutchings and Hibler, 2008). The ice deformation and its length scaling law in the south of the PAO during March–May have been estimated before by Hutchings et al. (2011 and 2018) and Itkin et al. (2017). Based on the dispersion characteristics of ice motion estimated using the data obtained from buoys deployed on the ice in the south of the Beaufort Sea, Lukovich et al. (2011) found that the scaling law of absolute zonal dispersion is about twice that at the meridional direction. Lei et al. (2020a and 2020b) used data recorded by two buoy arrays deployed in the north of PAO to describe the influence of cyclonic activities and summer ice regime on seasonal evolution in sea ice deformation.~~ However, the full picture of spatial and seasonal variations of sea ice kinematics and deformation for the whole PAO region has not been described using the buoy data in the previous literatures.~~ High resolution satellite images (e.g., Kwok, 2006) and sea ice numerical models (e.g., Hutter et al., 2018) have been ~~can be~~ used to identify spatial and temporal variations of ice deformation at the basin scale. RADARSAT data collected from the western Arctic Ocean reveals that the length scaling law of ice deformation would increase in summer as the ice pack weakens and internal stresses are not as readily transmitted over long distances as in winter (Stern and Lindsay, 2009). However, their ability to accurately characterize~~abilities to correctly describe~~ ice deformation, which usually occurs ~~in~~ on small scales and over short periods (Hutchings and Hibler, 2008), still requires more ground-truthing data by drifting buoys~~need ground-truthing data for example collected by buoys to assess~~. So far, a comprehensive picture of spatial and seasonal variations of sea ice kinematics and deformation for the

PAO region has not yet been obtained, and our understanding is particularly limited with respect to the transition from the melting season to a near rigid-lid ice pack in winter.

In order to address this knowledge gap,~~During August and September 2018,~~ 27 drifting buoys were deployed on sea ice in the PAO during August and September 2018 by the Chinese National Arctic Research Expedition (CHINARE) and the T-ICE expedition led by the Alfred-Wegener-Institute. In this study, w~~W~~e combined the data measured by these buoys ~~and~~ with other available buoy data from the International Arctic Buoy Programme (IABP) to identify the spatial variability of sea ice kinematic and deformation parameters in the PAO from melting to freezing season, and linked these results to the atmospheric forcing responsible for the observed changes in ice dynamics~~locate the atmospheric forcing parameters responsible to the ice dynamic changes~~.

2 Data and Methods

2.1 Deployment of drifting buoys

Four types of buoys were used in this study (Fig. 1). They are the Snow and Ice Mass Balance Array (SIMBA) buoy manufactured by the Scottish Association for Marine Science Research Services Ltd, Oban, Scotland~~,~~; the Snow Buoy (SB) designed by the Alfred-Wegener-Institute and manufactured by MetOcean Telematics, Halifax, Canada~~,~~; the ice Surface Velocity Program drifting buoy (iSVP) also manufactured by MetOcean Telematics~~,~~; and the ice drifter manufactured by the Taiyuan University of Technology (TUT), China. All buoys are equipped with GPS receivers providing a positioning accuracy of better than 5 m, and regularly reported their data to a land-based receiving station using the Iridium satellite network.

During the CHINARE, 9 SIMBA buoys and 11 TUT buoys were deployed in a narrow zonal section between 156° W and 171° W and a wide meridional range between 79.2° N and 84.9° N in August 2018 (Figs. 1 and 2). This deployment scheme was designed to facilitate the analysis of changes in ice kinematic~~ characteristicss~~ from the loose MIZ to the consolidated Pack Ice Zone (PIZ). ~~From~~ Of these 20 buoys, 15 were deployed in the northern part of the PAO as a cluster within close distance of each other (black circles in Fig. 2) to allow estimation of ice deformation rates. In addition, data from five SIMBAs and two SBs deployed by the T-ICE expedition in the Makarov Basin during September 2018 (Figs. 1 and 2) were also used to estimate ice deformation rates. Because the ice thickness at the deployment sites was comparably large (1.22 to 2.49 m), the buoys were able to survive ~~into~~ until winter and beyond. Position data from one iSVP deployed during the previous CHINARE in 2016 (Lei et al., 2020a) and four other IABP buoys were also included in this study. The IABP buoys were deployed by the British Antarctic Survey and Environment Canada in the east of the PAO during late August or late September 2018. Here we use the position data from these 32 buoys to describe spatial variations in ice kinematics (Fig. 2) between August 2018 and February 2019. We chose this study period because it represents ~~the~~ a transition ~~from late summer to winter, a~~ period during which the mechanical properties of sea ice are expected to change considerably (e.g., Herman and Glowacki, 2012; Hutter et al., 2018). Also, some buoys ~~have~~ ceased operation by March 2019. Two-thirds of the buoys (22) continued to send data until or beyond the end of the study period. The trajectories of the buoys during the study period covered the region of 76° N–87° N and 155° E–110°W, which we define here as our study region.~~which is defined as the study region~~~~To identify the spatial variability of atmospheric forcing and sea ice conditions, the study region is defined as 76° N–87° N and 155° E–110° W.~~

2.2 Analysis of sea ice kinematic characteristics

All buoys ~~have~~ had a sampling interval of either 0.5 or 1 h. Prior to the calculation of ice drift velocity, position data measured by the buoys were interpolated to a regular interval (τ) of 1 h. To quantify meridional (zonal) variabilities of ice kinematic properties, we used data from buoys that were within one standard deviation of the average longitude (latitude), which helps to minimize influence of zonal (meridional) difference on meridional (zonal) variabilities. This constraint ~~makes the~~leads to a meridional extent ranging from 350 to 402 km when the zonal variabilities of ice kinematics ~~was~~were assessed and a~~; while the~~ zonal extent ranging from 195 to 285 km for the assessment of meridional variabilities. Their seasonal changes can be considered as moderate (<40%) although the divergence of the buoys occurred at all times. If we use ~~the~~ half the standard deviations to constrain the calculation range, there would be no essential change in the identified meridional/zonal dependencies of ice kinematics from those obtained using one standard deviation. Thus, we consider our evaluation method ~~i~~as robust. Meridional variabilities ~~can be used to detect~~are related to the transition from the MIZ to the PIZ, while zonal variabilities ~~can~~ indicate the change between the region north of the Canadian Arctic Archipelago, where MYI coverage is usually large (Lindell and Long, 2016) and the Makarov Basin, which is mainly covered by seasonal ice (Serreze and Meier, 2018).

Two parameters were used to characterize sea ice kinematics. First, the IWSR was used to investigate the response of sea ice motion to wind forcing. Impacts of resampling data at intervals between 1 and 48 h, meridional and zonal spatial variabilities, intensity of wind forcing, near-surface air temperature, and ice concentration on the IWSR were assessed. These parameters are either related to spatiotemporal changes in atmospheric and sea ice conditions, or to the frequency characteristics of ice and wind speeds. The data used to characterize atmospheric forcing, including Sea Level air Pressure (SLP), near-surface air temperature at 2 m (T_{2m}) and wind velocity at 10 m (W_{10m}), were obtained from the ECMWF ERA-Interim reanalysis (Dee et al., 2011). Sea ice concentration was obtained from the Advanced Microwave Scanning Radiometer 2 (AMSR2) (Spreen et al., 2008). To identify the state of atmospheric forcing and ice conditions relative to the climatology, we also calculated anomalies of SLP, T_{2m}, W_{10m}, ice concentration, and ice drift speed relative to the 1979–2018 averages. To estimate ice concentration anomalies, we used ice concentration data from the Nimbus-7 Scanning Multichannel Microwave Radiometer (SMMR) and its successors (SSM/I and SSMIS) (Fetterer et al., 2017) because they cover a longer period than AMSR2 data. We used the daily product of sea ice motion (Tschudi et al., 2019 and 2020~~Fowler et al., 2013~~) provided by the National Snow and Ice Data Center (NSIDC) to estimate ice drift speed anomalies. Because of the delayed release of NSIDC data, ice drift speed anomalies were only estimated for August–December 2018.

Second, the inertial motion index (IMI) was used to quantify the inertial component of ice motion. To obtain the IMI, we applied a Fast Fourier Transformation to normalized hourly ice velocities. Normalized ice velocities were calculated by scaling velocity values to monthly averages, allowing seasonal change to be assessed independently of magnitudes of ice velocities. The frequency of the inertial oscillation varies with latitude as follows:

$$f_0 = 2\Omega \sin\theta \qquad (1)$$

where f_0 is inertial frequency, Ω is Earth rotation rate, and θ is latitude. ~~The~~ f_0 ranges from 2.01 to 1.94 cycles day^{-1} between 90° N and 75° N. Rotary spectra calculated from sea ice velocity using complex Fourier analysis were used to identify signals of inertial and tidal origin, both of which have a frequency of ~ 2 cycles day^{-1} in the Arctic Ocean (Gimbert et al., 2012). According to Gimbert et al.

(2012), the complex Fourier transformation $\widehat{U}(\omega)$ is defined as:

$$\widehat{U}(\omega)=\frac{1}{N}\sum_{t=t_0}^{t_{end}-\Delta t} e^{-i\omega t}\left(u_x+iu_y\right), \tag{2}$$

where N and Δt are the number and temporal interval of velocity samples, t_0 and t_{end} are the start and end times of the temporal window, u_x and u_y are zonal and meridional ice speeds at $t+0.5\Delta t$ on an orthogonal geographical grid, and ω is angular frequency. The IMI was defined as the amplitude at the negative-phase inertial frequency, i.e., $-f_0$, ~~–~~after the complex Fourier transformation. We note that~~,~~ the energies contributed to the amplitude at $-f_0$ comprise the potential contributions from quasi-semidiurnal inertial and tidal oscillations~~,~~ and the high-frequency components of wind and oceanic forcing; while that in the positive phase excludes contributions from inertial oscillation, and only comprises other components compared to~~as~~ that in a negative phase. This is because the spectral peaks associated with the tidal oscillation are roughly symmetric at positive and negative phases as a first order approximation (Gimbert et al., 2012). On the contrary, the spectral peak associated with the inertial oscillation is asymmetric~~,~~ and only occurs in the negative phase in the Arctic Ocean. Thus, we can identify the seasonal changes in the contributions of inertial oscillation by comparing the amplitude at the negative-phase quasi-semidiurnal frequency, i.e., IMI, with that in the positive phase (~~H~~hereinafter referred to as positive-phase amplitude, short: PHA~~ for short~~). Such method to separate the inertial oscillation from the tidal oscillation has been used by Lammert et al. (2009), who attempted to identify cyclone-induced inertial ice oscillation in Fram Strait. The background noise originat~~ed~~ing from high-frequency components of wind and oceanic forcing can shift the local maximums slightly from the targeted frequencies of IMI and PHA (Geiger and Perovich, 2008). Thus, we identify the local maximum amplitude in the range of $-f_0\pm0.03$ for the IMI and in the range of 2 ± 0.03 for the PHA. From artificial identification, such ranges can ensure almost all quasi-semidiurnal signals won't be missed. If no local maximum can be identified within the defined ranges, we use the amplitudes at $-f_0$ and 2 as the IMI and PHA. Such situation is ~~sparser~~rare for the IMI, i.e., approximately with 15% cases; while it is prevalent for the PHA, i.e., approximately with 95% cases. This implies an inertial oscillation is prevalent, while the tidal oscillation can be ignored regardless of season~~s~~ and buoy under consideration~~s~~, which might be related to the fact that all the buoys drifted over the deep waters beyond the continental shelf through the study period.

2.3 Analysis of sea ice deformation characteristics

Ice positions were used to estimate differential kinematic properties (DKPs) of the sea ice deformation field. The DKPs include divergence ~~rate~~ (*div*), shear ~~rate~~ (*shr*), and total deformation ~~rate~~ (*D*) rates of sea ice estimated within the area enclosed by any three buoys as Itkin et al. (2017). Following Hutchings and Hibler (2008), DKPs were calculated as follows:

$$div = \frac{\partial u}{\partial x} + \frac{\partial v}{\partial y} \ , \tag{3}$$

$$shr = \sqrt{\left(\frac{\partial u}{\partial x} - \frac{\partial v}{\partial y}\right)^2 + \left(\frac{\partial u}{\partial y} + \frac{\partial v}{\partial x}\right)^2} \ , \tag{4}$$

and $D = \sqrt{div^2 + shr^2}$, (5)

where $\frac{\partial u}{\partial x}$, $\frac{\partial v}{\partial y}$, $\frac{\partial u}{\partial y}$, and $\frac{\partial v}{\partial x}$ are the strain components on an orthogonal geographical grid. Sea ice strain rate was estimated only for buoy triangles with internal angles in excess of 15° and for ice speeds > 0.02 m s^{-1} to ensure a high accuracy (Hutchings et al., 2012). Total deformation *D* was used to characterize the spatial and temporal scaling laws as follows:

$$D \propto L^{-\beta}, \tag{6}$$

and $D \propto \tau^{-\alpha}$, (7)

where *L* is the length scale, τ is the sampling interval, and β and α are spatial and temporal scaling exponents~~,~~ which indicate decay rates of the sea ice deformation in spatial or temporal domains. These scaling laws can only indicate the fractal properties of the first moment of ice deformation because of the multi-fractal properties of ice deformation (Marsan et al., 2004; Hutchings et al., 2011 and 2018). To estimate the spatial exponent β, the length scale was divided into three bins of 5–10, 10–20, and 20–40 km for the CHINARE buoy cluster because only few samples were outside these bins. To the estimate temporal exponent α, the position data were resampled at intervals of 1, 2, 4, 8, 12, 24, and 48 h. Because the T-ICE buoy cluster was mostly (> 70 %) in the bin of 40–80 km, data from this cluster were ~~unsuitable~~ not suitable for the estimation of the scale effect. A s~~S~~pace–time coupling index, *c*, denoting temporal (spatial) dependence of the spatial (temporal) scaling exponent, can be expressed as:

$$\beta(\tau) = \beta_0 - c\ln(\tau), \tag{8}$$

where β_0 is a constant. The areal localization index, $\delta_{15\%}$, was used to quantify the localization of the strongest sea ice deformation, which is defined as the fractional area accommodating the largest 15 %

of the ice deformation in the research domain (Stern and Lindsay, 2009). The $\delta_{15\%}$ was calculated for the length bin of 10–20 km for the CHINARE buoy cluster because this bin contained more samples to ensure statistical rationality~~most of the samples~~. To identify the influence of the temporal scale on the localization of ice deformation, all data were resampled ~~at~~ to intervals of 1, 2, 4, 8, 12, 24, and 48 h.

2.4 Atmospheric circulation pattern

To identify the influence of atmospheric circulation patterns on sea ice kinematics and deformation, we calculated the seasonal Central Arctic Index (CAI) and DA index to relate to the potential of ~~the~~ sea ice advection ~~of sea ice~~ from the study region to the ~~Atlantic sector of the Arctic Ocean~~AAO (Vihma et al., 2012; Bi et al., 2019), and the seasonal AO and BH indices to relate to the strength of the BG (Lei et al., 2019). Monthly SLP data north of 70° N obtained from the NCEP/NCAR reanalysis I were used to calculate the empirical orthogonal functions ~~modes~~ (EOF), with the AO and DA as the first and second modes of EOF (Wang et al., 2009). The CAI was defined as the difference in SLP between 90° W and 90° E at 84° N (Vihma et al., 2012). The BH index was calculated as the average SLP anomaly over the domain of 75° N–85° N, 170° E–150° W (Moore et al., 2018) relative to 1979–2018 climatology.

3 Results and discussions

3.1 ~~Spatiotemporal~~ Spatial and seasonal changes in atmospheric and sea ice conditions

The BH index for autumn (September, October, and November) 2018 was moderate, ranking the tenth highest in 1979–2018 (Fig. 3a). However, the BH index for the following winter (December, January, and February) was much lower at −5.6 hPa, ranking the fourth lowest in 1979–2018 (Fig. 3b). Both, CAI and DA, were positive in autumn 2018, but still within one standard deviation of the 1979–2018 climatology ~~climatological values~~ (Fig. 3c and 3e). However, both ~~CAI and DA~~ were strongly positive in winter 2018/19, ranking the third and second highest in 1979–2018, respectively (Fig. 3d and 3f). Sea ice in the PAO is expected to be impacted considerably by these seasonal changes in atmospheric circulation patterns as a result of the northward advection of sea ice to the ~~Atlantic sector of the Arctic Ocean~~AAO (e.g., Bi et al., 2019). As an example, extreme sea ice reduction ~~conditions have~~ has been observed in the Bering Sea in late winter 2019, where sea ice extent was 70 %–80 % lower than normal (Perovich et al., 2019).

Associated with the seasonal change in the BH index, there was a distinct contrast in the pattern of the

BG between autumn and winter. Wind vectors and ice drift trajectories during autumn 2018 were generally clockwise, while those during the following winter were counterclockwise, with all buoys drifting northeastward from December 2018 onward and integrating into the TDS, i.e., from anticyclonic to cyclonic patterns (Fig. 4). In autumn 2018, strong northerly winds only appeared in the northwestern part of study region (Fig. 4a), and were associated with moderately positive CAI and DA. However, in winter 2018/2019, enhanced northerly winds prevailed almost across the entire study region (Fig. 4b), and were associated with extremely positive CAI and DA. The T_{2m} anomalies averaged over the study region ~~was~~ were 3.9 °C in autumn and 0.7 °C in winter (Fig. 4c and 4d), ranking the second and eleventh highest in 1979–2018, respectively.

The CHINARE buoys were deployed within a narrow meridional section at about 170° W. On 20 August 2018, sea ice concentration in this section, especially in the southern part, was considerably lower than that in the eastern part of the study region at about 120° W where other buoys had been deployed (Fig. 5a). Subsequently, ice concentration increased considerably, with almost all buoys being located in the PIZ by 20 September 2018 (Fig. 5b). However, the CHINARE buoys in the south and all T-ICE buoys remained within 70 km of the ice edge, ~~because~~ which~~it~~ retreated further during August–September 2018. By 20 October 2018, ice concentration surrounding all buoys had increased to over 95 % (Fig. 5c).

In September and early October 2018, ice concentrations were considerably lower than the 1979–2018 average. Ice concentrations increased after early October and became comparable with climatological values (Figs. 6b and 7b). In October 2018, ice concentration was much lower in the southern and western parts of the study region ~~than~~ compared to~~in~~ the north and east. Subsequently, the spatial gradient ~~heterogeneity~~ of sea ice concentration gradually decreased. Compared with 1979–2018 climatology, wind speed over the study period was lower during most of the time except for episodic increases as a result of intrusions of low-pressure systems (Figs. 6c and 7c). ~~The study region was dominated by low SLP during December 2018 and February 2019, which resulted in an anomalously low BH index and subsequent increases in both wind and ice drift speeds (Figs. 6c, 6d, 7c, and 7d).~~ In September 2018, ice speed in the south was higher than that in the north (Fig. 6d), ~~implying that~~suggesting that the sea ice response to wind forcing was stronger in the south because of the lower ice concentration. From October 2018 onwards, this north–south difference gradually disappeared. The study region was dominated by low SLP during December 2018 and February 2019, which ~~resulted~~

~~in~~was related to an anomalously low BH index and subsequent increases in both wind and ice drift speeds (Figs. 6c, 6d, 7c, and 7d).

3.2 Spatial and seasonal changes in ~~S~~sea ice kinematic characteristics

Temporal resampling has little effect on wind speed. However, applying longer resampling intervals to buoy position data may filter out ice motions at higher frequencies (Haller et al., 2014), resulting in reduced ice speed and IWSR (Fig. 8). For example, ice drift speed and IWSR in September 2018 were 0.13 m s^{-1} and 0.027 at a resampling interval of 1 h, and decreased to 0.01 m s^{-1} and 0.021 at a resampling interval of 48 h. Both ice speed and IWSR decreased considerably from September to November 2018; afterwards, both variables remained low until the end of the study period. At a resampling interval of 6 h, the IWSR was 0.026 in September 2018 (Fig. 8), which is much lower than that (0.013) obtained in the region close to North Pole in the same month of 2007 (Haller et al., 2014) because most parts of our study region ~~involves~~ included the MIZ at that time. This value decreased to 0.008–0.015 during November to February (Fig. 8), which is comparable ~~with~~ to those obtained from the regions north of Siberia or Greenland and the region close to North Pole during the freezing season, but much smaller than that obtained from Fram Strait (Haller et al., 2014). This implies that, during the freezing season, the response of sea ice to wind forcing is relatively uniform for the entire Arctic Ocean except for the strait regions where ice speed increases obviously. In January 2019, a~~A~~ more consolidated ice pack and relatively weak wind forcing led to both ice drift speed and IWSR reaching minima~~ums~~ for the entire study period~~ in January 2019~~ (Figs. 6c and 7c). The e~~E~~ffect of resampling on the IWSR was considerably reduced during the freezing season, implying remarkable reductions of meandering and sub-daily oscillations in ice motion during the freezing season. The ~~R~~ratio between IWSRs at 1-h and 48-h intervals in October was 70 % of that in September. This ratio remained almost unchanged between November and February.

Factors regulating the ~~impacting~~ IWSR are summarized in Table 1. The ~~I~~impact of the geographical location was significant in autumn, ~~resulting in~~with relatively high IWSRs in the southern or western parts of the study region. However, meridional changes in the IWSR ~~impact of latitude~~ became very ~~slight~~ small in January–February because the north–south gradient in ice conditions was negligible by that time. The west–east gradient was more pronounced, ~~resulting in~~with a significant relationship between longitude and IWSR through the study period~~from autumn until February~~. This is consistent with the results given by Lukovich et al. (2011), who identified that the west–east gradient of sea ice motion is larger than that in the north–south direction for the south of PAO during the freezing season. In summer and early autumn, consolidation of the ice field is low, and interactions between ice floes approximate rigid particle collisions (Lewis and Richter-Menge, 1998). Thus, in August–October 2018, a lower IWSR ~~in August–October 2018~~ is related to stronger wind forcing that strengthened interactions between floes~~. Under the weak wind forcing, the inertial component of ice motion would increase and the IWSR would increase~~, which ~~also~~ leads to a significant negative statistical ~~negative~~ correlation between IWSR and wind speed. Similarly, based on the data obtained from the buoys deployed in the TDS region, Haller et al. (2014) also ~~found~~ identified that ~~the~~ some spikes of the IWSR tend to be ~~were~~ associated with ~~the~~ a low wind speed. Consolidation of the ice field between November and February 2018 ~~leaded~~ led to reduced ice motion and weaker sea ice response to wind forcing. Thereby, impact of wind forcing on IWSR was insignificant from November onwards. Variations of T_{2m} across the study region between 20 August and 30 September 2018 were relatively small (−1.7 to −3.5 °C) because of the thermodynamic equilibrium between sea ice and the atmosphere during the melt season (e.g., Screen and Simmonds, 2010). The statistical relationship between T_{2m} and the IWSR was insignificant during this period. However, the relationship became significant during October–December 2018, with higher T_{2m} being associated with a higher IWSR because warmer conditions may have weakened ice pack (Oikkonen et al., 2017). As continued thickening of the ice cover further reduced the influence of air temperature on ice motion, the statistical relationship between T_{2m} and the IWSR was insignificant in January and February 2019.

~~The inertial oscillation of ice motion is stimulated by sudden changes in external forces, majorly due to enhanced wind forcing (Gimbert et al., 2012). It was weakened due to kinetic energy dissipation because of surface friction and internal ice stresses.~~The initial strength of the inertial oscillation mainly depends on the wind stress. However, the sustainability of inertial oscillation is restricted by the internal friction within the Ekman ocean layer in the region with low ice concentration or open waters, or by the ice internal stress in the PIZ (Gimbert et al., 2012). The inertial component of ice motion is closely associated with the seasonal and spatial changes in ice conditions. Figure 9 shows monthly IMI and PHA obtained from each buoy displayed at the midpoint of the buoy's trajectory for different months. Average IMI of all available buoys for the study period was 0.~~090~~099 ± 0.~~065~~088, with the average for September 2018 (0.~~209~~227) being considerably higher. Monthly average IMI from all buoys decreased from 0.~~108~~ 136 in October 2018 to 0.~~035~~ 037 in February 2019. Spatial variability of the IMI had almost disappeared by February 2019; IMI standard deviation in February 2019 was ~~12~~ 13 %–~~20~~ 22 % of that in September–October 2018. Both the magnitude and the spatiotemporal variations of the PHA were much smaller than those of the IMI. The average PHA of all available buoys for the study period was only 18% of the IMI. The monthly ratio between PHA and IMI ranged from 0.06 in September 2018 to 0.46 in February 2019. The seasonal damping of this ratio is mainly due to the decrease in the IMI because no statistically significant trend can be identified for the PHA. The standard deviation of the IMI reveals a significant decreaseing trend from 0.069–0.117 in September–October to 0.015 in February, which suggests ~~implies~~ that the spatial variation of the IMI gradually decreased as winter approaching. Similar with the ratio between the absolute magnitudes, the ratio between the standard deviations of PHA and IMI increased from 0.08 in September to 0.50–0.70 in January–February. The seasonal increase in this ratio also was mainly due to the ~~seasonal~~ decrease in the standard deviation of the IMI. Thus, from comparisons between the seasonalitiesy of IMI and PHA, we can infer that, the seasonal changes and spatial variations in the IMI could be mainly related to the ~~seasonality~~changes in ~~of~~ inertial oscillation, and the contributions of tidal oscillation can be ignored through the study period.–

The analysis of the IMI for the entire PAO reveals that its seasonal change mainly occurs in the seasonal ice region. On the contrary, that in the pack permanent ice region is almost negligible, which implies that the inertial oscillation initialized by wind stress will be attenuated rapidly by the ice internal stress in the PIZ regardless of season. To eliminate the influence of large-scale spatial variability, we inspected subsets of data obtained from buoys deployed in clusters. The IMI obtained from the CHINARE buoy cluster (black circles in Fig. 2) decreased markedly from 0.~~213~~ 223 to 0.~~071~~ 081 during September–October 2018. However, a similar change was observed one month later in October–November 2018 for the T-ICE buoy cluster. During the freezing season from November to February, the IMI gradually decreased to 0.~~036~~ 038 for the CHINARE cluster and to 0.~~032~~ 035 for the T-ICE cluster. Sea ice growth rate of the thin ice in the MIZ in the western and southern parts of the study region is expected to be higher than that in the PIZ in the north or the east (e.g., Kwok and Cunningham, 2008). Accordingly, the spatial variability of ice inertial oscillation observed in early autumn gradually disappeared.

3.3 Spatial and seasonal changes in ~~S~~sea ice deformation

For all the buoy triangles used to estimate ice deformation, ice concentration within the CHINARE buoy cluster increased rapidly during late August and early September 2018, and it remained close to 100 % from then onwards (Fig. 10a). However, a comparable seasonal increase in ice concentration within the T-ICE buoy cluster was observed one month later. To facilitate direct comparison of data obtained from two buoy clusters, we estimated ice deformation rate of the T-ICE buoy cluster at the 10–20 km scale using the value at the 40–80 km scale and a constant spatial scaling exponent of 0.55. The scaling exponent of 0.55 is a seasonal average obtained from the CHINARE buoy cluster. A change of the scaling exponent by 10 % would lead to an uncertainty of about 0.03 for the ice deformation rate. Thus, a constant scaling exponent can be considered acceptable for a study of seasonal variation. In early and mid-September 2018, ice deformation rate was low for the CHINARE cluster (Fig. 10b) because of low wind speed and relatively stable ~~infrequent changes in~~ wind direction, and despite a weakly consolidated ice field (Fig. 2). For the T-ICE cluster, both ice deformation rate and ratio between ice deformation rate and wind speed decreased rapidly between 20 September and 10 November 2018, associated with consolidation of the ice field as ice concentration and thickness increased and temperature decreased. However, ice deformation rate from the CHINARE cluster decreased only slightly over the same period, which is likely because its initial deformation rate was relatively low in late September 2018, and associated with the higher ice concentration in the CHINARE region ~~in late September 2018 was higher~~ than that in the T-ICE region by 15 %–20 %.

For the CHINARE buoy cluster, daily wind speed can explain 35 % (P<0.001) of the daily ice deformation rate estimated using hourly position data over the study period. However, for the T-ICE cluster ~~between September and early November 2018~~, changes in ice deformation were mainly regulated by the seasonal evolution of ice concentration between September and early November 2018. The relationship between ice deformation rate and wind speed was insignificant at the statistical confidence level of 0.05 during this period. The ice field had sufficiently consolidated by mid-November 2018, and the relationship between daily ice deformation rate and daily wind speed changed to significant (R^2 = 0.12, P<0.01) from then onwards.

The a~~A~~verage ratio of ice deformation rate to wind speed in autumn was 1.15 × 10^{-6} m^{-1} for the CHINARE cluster and 0.62 × 10^{-6} m^{-1} for the T-ICE cluster; the ratio in winter decreased to 0.86 ×10^{-6}

and 0.17 × 10^{-6} m^{-1}, respectively. This is consistent with results of Spreen et al. (2017), who ~~by~~ used~~ing~~ the RGPS data to reveal~~, which showed~~ that the ~~–~~annual maximum ice deformation rate occurred in August, and decreased gradually to the annual minimum in March. Except for late September 2018, when ice concentration in the T-ICE cluster was less than 85 %, ice deformation rate from the CHINARE cluster was generally larger than that from the T-ICE cluster, with average values of 0.45 and 0.13 d^{-1}, respectively, for October 2018 to February 2019. Sea ice in the region of the T-ICE cluster was generally thinner than that in the region of the CHINARE cluster. Thus, the difference in ice deformation rate cannot be explained by difference of ~~between~~ ice conditions between ~~in~~ the two regions, and is most likely ~~attributed~~ related to spatial heterogeneity and temporal variability of wind and/or oceanic forcing. ~~The CHINARE cluster was located in the core region of the BG; thus, vorticity of the surface current must be greater than that in the T-ICE cluster, which was located at the western boundary of the BG (Armitage et al., 2017).~~ ~~Furthermore, c~~Changes in the direction of wind vectors were more frequent around the CHINARE cluster than around the T-ICE cluster. Frequent changes in ice drift direction lead to larger ice deformation, such as the events on 11 October, and 11 and 26 November 2018 for the CHINARE cluster as shown in Fig. 10b. The d~~D~~rifting trajectories~~y~~ of the T-ICE cluster ~~was~~ were much straighter than ~~that~~ those of the CHINARE cluster. Furthermore, ~~T~~the CHINARE cluster was located in the core region of the BG; thus, vorticity of the surface current must be greater than that in the T-ICE cluster, which was located at the western boundary of the BG (Armitage et al., 2017). As a result, ice deformation rate and its ratio to wind speed were lower for the T-ICE cluster than for CHINARE cluster.

Ice deformation rates obtained from the CHINARE buoy cluster at three representative lengths of 7.5, 15, and 30 km were estimated using Eq. (6). ~~Influence of synoptic processes, e.g., cyclonic activities and/or changes in wind direction, was filtered out by using a monthly window.~~ Figure 11 shows that monthly average ice deformation decreased as length scale and resampling interval increased, implying ice deformation localization and intermittency. Ice deformation decreased rapidly at all spatial and temporal scales during the seasonal transition period of September–October, and remained low from then onwards. Ice deformation rate obtained ~~from~~ using hourly position data from the CHINARE buoy cluster in September 2018 was 0.38 d^{-1} at the length scale of 30 km, which is comparable with that in September 2016 (0.31 d^{-1}), and much larger than that in September 2014 (0.18 d^{-1}) observed also in northern PAO (Lei et al., 2020b). These observed differences can be ~~attributed~~ related to the strong storms in late September 2018 (Fig. 10b) and early September 2016 (Lei et al., 2020b), in contrast ~~withas well as~~ to the relatively stable synoptic conditions and relatively compact ice conditions in September 2014 (Lei et al., 2020b).

Accordingly, ~~The~~ the spatial scaling exponent β estimated from hourly position data was 0.61 in September 2018, and is comparable with that from September 2016 (0.60), but slightly larger than that in September 2014 (0.46) observed in northern PAO (Lei et al., 2020b). The value of β decreased markedly from September to October 2018, and varied little from then onwards (Fig. 12). With increases in ice thickness and concentration and cooling of the ice cover from October onwards, consolidation of the ice field is enhanced, and sea ice deformation can spread over longer distances ~~from October onwards~~. By February 2019, the spatial scaling exponent β from hourly position data decreased to 0.48, which is comparable with that (0.43) obtained from February 2015 in the northern PAO (Lei et al., 2020a). This suggests ~~implies~~ that~~y~~ the year-to-year changes in the spatial scaling of ice deformation during winter are~~is~~ not as strong as that in early autumn, which is ~~similar~~ in line with the change pattern of ice thickness (e.g., Kwok and Cunningham, 2008). The value of β decreased exponentially with the increase in sampling frequency for all months, which indicates the spatial scaling would be underestimated with the observations of coarsened ~~observation~~ temporal resolution. The β interpolated to 3 h was 0.42 and 0.44 in January and February 2019, respectively, which is comparable with that (0.40) obtained from south of the PAO during March–May (Itkin et al., 2017). The ice growth season generally lasts to May–June in the PAO (Perovich et al., 2003), which implies the consolidation of sea ice in March–May is comparable to, or even stronger than, that in January–February. Thus, the β derived from our results is essentially consistent with that given by Itkin et al. (2017). The β extrapolated to 48 h (120 h) decreased to 0.29 (0.25) in January and 0.33 (0.28) in February 2019, respectively, which was comparable with that (0.20) obtained from the estimations using RADARSAT images with temporal resolution of 48–120 h during the freezing season for the pan Arctic Ocean (Stern and Linday, 2009). We further use the seasonal bin to test the sensitivity of the estimation of β to the number of samples. Consequentially, the seasonal β was estimated at 0.54 and 0.48 for autumn and winter, respectively, which is close to those (0.53 and 0.49) averaged directly from the monthly values. Therefore, we believe that the monthly segmentation for estimations of β is statistically appropriate and can better reveal seasonal changes.

The temporal scaling exponent α also exhibited a strong dependence on the spatial scale, which means relatively large intermittency of ice deformation can be obtained by fine-scale observations (Fig. 13). Seasonally,~~T~~ the value of α decreased between September and October 2018 because of enhanced consolidation of the ice cover. The value of the space–time coupling coefficient c increased monotonously from 0.034 in autumn to 0.062 in winter, suggesting gradual enhancement of the brittle rheology of the ice cover. This is consistent with the results derived from RADARSAT images (Stern and Moritz, 2002), which revealed that sea ice deformation is more linear in winter, and more clustered and spatially random in summer. The value of c in September 2018 is comparable with that in September 2016 (0.03). However, it is only about half that in September 2014 (0.06) (Lei et al., 2020b) because of the different ice conditions. The value of c in January–February 2019 (0.059–0.062) is comparable with the values obtained in January–February 2015 (0.051–0.077) from the northern PAO (Lei et al., 2020a), and the value obtained from the region north of Svalbard in winter and spring (Oikkonen et al., 2017).

The areal localization index denotes the area with the highest deformation. It had a strong dependence on the temporal scale, and increased linearly ($P<0.001$) as the logarithm of the temporal scale increased (Fig. 14), which implies that the localization of ice deformation would be underestimated by the observations or models with coarser resolution. Seasonally, the a~~A~~real localization index decreased ~~markedly~~ remarkably from September to November 2018, indicating that ice deformation was increasingly localized during the transition from melting to freezing. During the freezing season, the ice deformation mainly occurs ~~is concentrated~~ along linear cracks, leads, and/or ridges, which is related to a high localization; while during melt season, the ice deforming zones are in clumps rather than along lines, and the spatial distribution of ice deformation rate is more even and amorphous, which is related to a low localization. During freezing season from November to February~~However~~, the degree of deformation strongly regulated the localization of ice deformation, with the monthly ice deformation rate explaining 96 % of the monthly areal localization index ($P<0.01$)~~ during November–February~~. This means that extremely high ice deformation can spread over longer distances. The a~~A~~real localization index for January–February 2019 corresponding to a temporal resolution of 1 h and a length scale of 10–20 km was 1.9 %–2.3 %, which was close to the value (1.6%) estimated at scale of 13–20 km (Marsan et al., 2004), and that (1.5%) at a scale of 10 km (Stern and Lindsay, 2009) using RADARSAT images, as well as that (2.4 %–2.7 %) estimated at ~~the~~ a length scale of 18 km using a high resolution numerical model (Spreen et al., 2017). We further analyze ~~use~~ other fractional areas accommodating the largest 10 % or 20% of the ice deformation. Although the adjusted indices would have different magnitudes, their patterns of seasonal change ~~patterns~~ and the linearly dependence on the logarithm of the temporal scale are consistent as those obtained using the threshold of 15%. Therefore, the understanding of the localization of the ice deformation derived from this study is not very sensitive to the selected threshold.

3.4 Spatial differences in the trends of sea ice loss in the PAO and their implications for sea ice kinematics and deformation

~~Summer i~~Sea ice conditions in the melt season have profound effects on sea ice dynamic and thermodynamic processes in the following winters. For example, e~~E~~nhanced divergence of summer sea ice leads to increased absorption of solar radiation by the upper ocean and delays onset of ice growth (e.g., Lei et al., 2020b). As shown in Fig. 15, the long-term decrease of sea ice concentration in the first half of September, when Arctic sea ice extent reaches its annual minimum (Comiso et al., 2017), is stronger in the southern and western parts of the study region than in the north and the east. The western and southern parts of the study region have become ice free in September during recent years. On the contrary, there is no significant trend in ice concentration in the first half of September along the trajectory of the easternmost buoy (Fig. 15e). This suggests that, the melting period is getting longer in the southern and western parts of the PAO compared to the north and east. Consequently, the spatial gradient of ice thickness in the PAO, especially during autumn and early winter, will be further enhanced through delaying the onset of ice growth and reducing ice thickness in the south and west. At the end of the freezing season, the enhanced ice deformation will promote the sea ice breaking up and expand the MIZ northward, which is conducive to the advance of the melt season. Thus, the north–south and east–west differences in sea ice kinematics are likely to be more pronounced in the future.

~~Multi-year ice in the Pacific and eastern sectors of the Arctic Ocean is being gradually depleted (Serreze and Meier, 2018), resulting in the domination of seasonal sea ice. Consequently, a deformation of the ice field creates unfrozen first-year ice ridges (Salganik et al., 2020). These new~~

~~ridges, together with the newly formed thin ice in leads, are mechanically vulnerable components of the ice field, and predispose the ice field to further deformation under external forces. The drifting ice camp of the international Multidisciplinary drifting Observatory for the Study of Arctic Climate (MOSAiC) has just finished an operation for a year (2019–2020) from the region north of the Laptev Sea (Krumpen et al., 2020), which is to the west of the T-ICE buoy cluster. Ice thickness around the MOSAiC ice station is much lower (Krumpen et al., 2020) than that in the areas of the buoy clusters included in this study. Frequent sea ice breaking has been observed around the central observatory of MOSAiC during the drifting. Thus, data and results from this study can be used as a proxy baseline for comparing and investigating deformation of the MOSAiC ice pack.~~

~~4 Discussions~~

~~The pronouncedH high intermittence of ice deformation implies that an episodic opening or closing of the sea ice cover may be undetectable in from data with longer sampling intervals, such as remote sensing data with resolutions of one or two days. Consequently, fluxes of heat (e.g., Heil and Hibler, 2002) or particles and gases (e.g., Held et al., 2011) released from these openings in the PIZ to the atmosphere would be underestimated if they are derived from remote sensing products. Thishighlightsing the importance of using data with higher temperal resolution to characterize sea ice deformation accurately. Our results also show that ice deformation intermittence is underestimated at longer spatial scales. This is consistent with results from numerical models, which indicate that the most extreme deformation events may be absent in the output of models with lower spatial resolution (Rampal et al., 2019). This emphasizes , emphasizing the need for high-resolution sea ice dynamic models to reproduce linear kinematic features of ice deformation (e.g., Hutter and Losch, 2020). Dependence of the ratio of ice speed to wind speed on resampling frequency implies that temporal resolution should be considered carefully when using wind forcing data to parameterize or simulate sea ice drift.~~

~~The PAO is the region with the most significant summer sea ice loss across the entire Arctic Ocean (Comiso et al., 2017). Summer ice conditions have profound effects on sea ice dynamic and thermodynamic processes in the following winters. Pronounced loss of sea ice in the southern and western parts of the study region resulted in an inertial signal and ice motion response to wind forcing that were stronger than those found to the north and the east. As shown in Fig. 15, the long-term~~

~~decrease of sea ice concentration in the first half of September, when Arctic sea ice extent reaches its annual minimum (Comiso et al., 2017), is more obvious and significant in the southern and western parts of the study region than in the north and the east. The western and southern parts of the study region have become ice free in September during some years recently. On the contrary, there is no significant trend in ice concentration in the first half of September along the trajectory of the easternmost buoy (Fig. 15e). This implies thatas sea ice loss continues in the western and southern parts of the study region, north-south and east-west differences in sea ice kinematics are likely to be enhanced.~~

~~Multi-year ice in the Pacific and eastern sectors of the Arctic Ocean is being depleted gradually (Serreze and Meier, 2018), resulting in the domination of seasonal ice. Consequently, a deformation of the ice field creates unfrozen first-year ice ridges (Salganik et al., 2020). These new ridges, together with the newly formed thin ice in leads, are mechanically vulnerable parts of the ice field, and predispose the ice field to further deformation under external forces. The ice drifting station of the international Multidisciplinary drifting Observatory for the Study of Arctic Climate (MOSAiC) has been designed to operate for a year (2019-2020) from the region north of the Laptev Sea (Krumpen et al., 2020), which is to the west of the T-ICE buoy cluster. Ice thickness around the MOSAiC ice station is much lower (Krumpen et al., 2020) than that in the areas of the buoy clusters included in this study. Frequent sea ice breaking has been observed around the central observatory of MOSAiC during the drifting. Thus, data and results from this study can be used as a proxy baseline for comparing and investigating deformation of the MOSAiC ice pack.~~

~~In this study, we examined atmospheric influences on sea ice kinematics and deformation. The ocean also plays an important role on ice drift and deformation, especially at mesoscales, greatly enhancing ice motion nonuniformity and ice deformation (e.g., Zhang et al., 1999). In the PAO, mesoscale ocean eddies prevail over the shelf break and the Northwind and Alpha-Mendeleyev Ridges (e.g., Zhang et al., 1999, Zhao et al., 2016). To characterize the influence of mesoscale oceanic eddies on ice deformation, observations from ice-drifter arrays are insufficient, highlighting the need to combine deployment of ocean-profiler arrays as part of the distributed network of MOSAiC (Krumpen et al., 2020).~~

~~5~~ 4 Conclusion and outlook

High-resolution position data recorded ~~measured~~ by 32 ice-based drifting buoys in the PAO between August 2018 and February 2019 were analyzed in detail to characterize spatiotemporal variations of sea ice kinematic and deformation properties ~~during autumn–winter of the 2018/19 ice season~~. During the transition from autumn 2018 to winter 2019, ice deformation and its response to wind forcing, as well as the inertial signal of ice motion gradually weakened. At the same time, space–time coupling of ice deformation was enhanced as the mechanical strength of the ice field increased. After a complex Fourier transformation, we found that the influence of tidal forcing on the quasi-semidiurnal oscillation of ice motion was negligible regardless of season because the buoys drifted over deep waters beyond the continental shelf. From this, we infer that the tidal forcing only plays a trivial role on ice deformation. During the freezing season between October 2018 and February 2019, ice deformation rate in the northern part of the study region was about 2.5 times that in the western part. This difference is likely related to the higher spatial heterogeneity of the oceanic and atmospheric forcing in the northern part of the study region, which lies in the core region of the BG. Because of seasonal change in the large-scale atmospheric circulation pattern, especially for the enhanced positive phases of the CAI and DA, a significant change in ice drift direction from anticyclonic to cyclonic patterns was observed in late November 2018, leading to temporal increases in both ice deformation rate and its ratio to wind forcing.

The pronounced high intermittence of ice deformation suggests that an episodic opening or closing of the sea ice cover may be undetectable from data with longer sampling intervals, such as remote sensing data with resolutions of one or two days. Consequently, fluxes of heat (e.g., Heil and Hibler, 2002) or particles and gases (e.g., Held et al., 2011) released from these openings in the PIZ to the atmosphere would be underestimated if they are derived from remote sensing products. The ~~D~~dependence of the ratio of ice speed to wind speed on resampling frequency also suggests ~~implies~~ that temporal resolution should be considered carefully when using wind forcing data to parameterize or simulate sea ice drift. From a spatial perspective, ~~This highlights the importance of using data with higher temporal resolution to characterize sea ice deformation accurately. O~~our results ~~also show~~reveal that ice deformation intermittence is underestimated at longer ~~spatial~~ scales. This is consistent with results from numerical models, which indicate that the most extreme deformation events may be absent in the output of models with lower spatial resolution (Rampal et al., 2019). This emphasizes the need for high-resolution sea ice dynamic models (e.g., Hutter and Losch, 2020) to reproduce linear kinematic features of ice deformation.

The response of ice kinematics to wind and inertia forcing was stronger in the south and west compared to the north and east of the study region, which is partly associated with the spatial heterogeneity of ice conditions inherited from previous seasons. During the transition from autumn to winter, the north–south and east–west gradients in the IWSR and inertial component of ice motion gradually decreased and even disappeared entirely, which is in line with the seasonal evolution of ice concentration and thickness. Spatial heterogeneity in ice conditions in autumn is likely to be amplified with increased loss of summer ice cover in the southern and western parts of the PAO, which is expected to further enhance the east-west and north-south differences in sea ice kinematics.

Multi-year ice in the Pacific and eastern sectors of the Arctic Ocean is being gradually depleted (Serreze and Meier, 2018), resulting in the domination of seasonal sea ice. Consequently, a deformation of the ice field in this region creates unfrozen first-year ice ridges (Salganik et al., 2020). These new ridges, together with the newly formed thin ice in leads, are mechanically vulnerable components of the ice field, and predispose the ice field to further deformation under external forces. The international Multidisciplinary drifting Observatory for the Study of Arctic Climate (MOSAiC) drift experiment ~~has just finished an operation for a year~~ (2019–2020) started from the region north of the Laptev Sea (Krumpen et al., 2020), which is to the west of the T-ICE buoy cluster. Ice thickness around the MOSAiC ice station ~~is~~was much lower (Krumpen et al., 2020) than that in the areas of the buoy clusters included in this study. Frequent sea ice breaking has been observed around the central observatory of MOSAiC during the drift~~ing~~. Data and results from the~~is~~ present study can be used as a proxy baseline for comparing and investigating deformation of the MOSAiC ice pack. By comparing our results to the observations from the MOSAiC buoy array, we may get a broader understanding of the spatial variation of sea ice deformation over the pan Arctic Ocean.

In this study, we only examined atmospheric influences on sea ice kinematics and deformation. The ocean also plays an important role on ice drift and deformation, especially on mesoscales, greatly enhancing ice motion nonuniformity and ice deformation (e.g., Zhang et al., 1999). In the PAO, mesoscale ocean eddies prevail over the shelf break and the Northwind and Alpha-Mendeleyev Ridges (e.g., Zhang et al., 1999, Zhao et al., 2016). To assess the influence of mesoscale oceanic eddies on ice deformation, observations from ice-drifter arrays are insufficient. This highlights the need for a complementary deployment of ocean-profiler arrays, which was for example realized recently as part of the distributed network of MOSAiC (Krumpen et al., 2020).

Deformation of sea ice creates ample opportunity for increased sea ice biological activities. Irradiance and nutrients, the two major limiting agents for biological growth in the sea ice realm (Ackley and Sullivan, 1994), are strongly impacted by sea ice deformation. For example, pressure ridges generally have large semi-enclosed chambers, which can provide more nutrients for biological activity (Ackley and Sullivan, 1994; Geiger and Perovich, et al., 2008). Sea ice deformation would also increase ice surface roughness, which in turn increases the potential of melt pond formation in early summer (e.g., Perovich and Polashenski, 2012). The formation of ponds leads to an increase in the transmission of irradiance through the ice cover and promote the biological growth (e.g., Nicolaus et al., 2012). In order to better understand the linkages between sea ice dynamical and biological processes, more joint observations are urgently needed.

Author contributions

RL is responsible for project coordination and paper writing. MH, BC, GZ, and GD undertook the processing and analysis of the buoy data, and interpretation of results. RL, WY, and JB deployed the buoys. The buoy data were provided by RL, MH, and BC. The ~~calculation of~~ atmospheric circulation index was ~~done~~ calculated by QC. All authors commented on the manuscript.

Data availability

The CHINARE buoy data are archived in the National Arctic and Antarctic Data Centre of China at https://www.chinare.org.cn/metadata/53de02c5-4524-4be4-b7bb-b56386f1341c (DOI: 10.11856/NNS.D.2020.038.v0). The T-ICE buoy data were archived in the online sea-ice knowledge and data platform at www.meereisportal.de. The IABP buoy data are archived at http://iabp.apl.washington.edu/index.html.

Competing interests

The authors declare that they have no conflict of interest.

Acknowledgments

We are most grateful to the Chinese Arctic and Antarctic Administration and the Alfred-Wegener-Institute for their logistical and financial support of the cruises of CHINARE and T-ICE, respectively. We thank the captains, crews and science parties of the R/V Xuelong and the Akademik Tryoshnikov, especially cruise leaders Dr. Zexun Wei and Dr. Benjamin Rabe, for their incredible support during the expeditions. The AMSR2 passive microwave ice concentrations were provided by the University of Bremen. The SMMR-SSMIS ice concentration and ice motion products, and the monthly Arctic Sea Ice Index were provided by the NSIDC. The ERA-Interim reanalysis was obtained from the ECMWF. Monthly sea level pressure is obtained from the NCEP/NCAR reanalysis I dataset. We are very grateful to the two anonymous reviewers and the responsible editor Dr. Ted Maksym for their comments, which have greatly improved our paper.

Financial support

This work was supported by grants from the National Key Research and Development Program (2018YFA0605903, 2016YFC1400303 and 2016YFC1401800) and the National Natural Science Foundation of China (41722605 and 41976219). B.C. was supported by the European Union's Horizon 2020 research and innovation programme (727890 – INTAROS) and Academy of Finland under contract 317999. The buoys deployed on T-ICE were funded by the Alfred-Wegener-Institute through the infrastructure programs FRAM and ACROSS.

References

Ackley, S.F., Sullivan, C.W.: Physical controls on the development and characteristics of Antarctic sea ice biological communities—a review and synthesis, Deep-Sea Research I 41 (10), 1583–1604, 1994.

Alam, A. and Curry, J. A.: Evolution of new ice and turbulent fluxes over freezing winter leads, J. Geophys. Res. Oceans, 103, 15783–15802, 1998.

Armitage, T. W. K., Bacon, S., Ridout, A. L., Petty, A. A., Wolbach, S., and Tsamados, M.: Arctic Ocean surface geostrophic circulation 2003–2014, The Cryosphere, 11, 1767–1780, https://doi.org/10.5194/tc-11-1767-2017, 2017.

Assmy, P., Fernández-Méndez, M., Duarte, P., and other coauthors: Leads in Arctic pack ice enable early phytoplankton blooms below snow-covered sea ice, Sci. Rep., 7:40850. https://doi.org/10.1038/srep40850, 2017.

Bi, H., Yang, Q., Liang, X., Zhang, L., Wang, Y., Liang, Y., and Huang, H.: Contributions of advection and melting processes to the decline in sea ice in the Pacific sector of the Arctic Ocean,. The Cryosphere, 13, 1423–1439, https://doi.org/10.5194/tc-13-1423-2019, 2019.

Geiger C. A., and Perovich D. K.: Springtime ice motion in the western Antarctic Peninsula region, Deep-Sea Res. II, 55, 338–350, 2008.

Comiso, J. C., Meier, W. N., and Gersten, R.: Variability and trends in the Arctic sea ice cover: results from different techniques, J. Geophys. Res. Oceans, 122, 6883–6900, doi:10.1002/2017JC012768, , 2017.

Dee, D. P., Uppala, S. M., Simmons, A. J., et al.: The ERA-interim reanalysis: configuration and performance of the data assimilation system, Quarterly Journal of the Royal Meteorological Society, 137, 553–597. https://doi.org/10. 1002/qj.828, 2011.

Ding, Q., Schweiger, A., L'Heureux, M., Battisti, D. S., Po-Chedley, S., Johnson, N. C., Blanchard-Wrigglesworth, E., Harnos, K., Zhang, Q., Eastman, R., and Steig, E. J.: Influence of high-latitude atmospheric circulation changes on summertime Arctic sea ice, Nature Clim Change, 7, 289–295, 2017.

Fetterer, F., Knowles, K., Meier, W. N., Savoie, M., and Windnagel, A. K.: Updated daily sea ice index, version 3, sea ice concentration, Boulder, Colorado USA. NSIDC: National Snow and Ice Data Center. doi: https://doi.org/10.7265/N5K072F8, 2017.

Fernández-Méndez, M., Olsen, L. M., Kauko, H. M., and other coauthors: Algal hot spots in a changing Arctic Ocean: sea-ice ridges and the snow-ice interface, Front Mar. Sci., 5: 75. https://doi.org/10.3389/fmars.2018.00075, 2018.

~~Fowler, C., Emery, W., and Tschudi, M.: Polar Pathfinder daily 25 km EASE-Grid sea ice motion vectors, version 2., edited. Boulder, Colorado USA: National Snow and Ice Data Center, 2013.~~

Gimbert, F., Marsan, D., Weiss, J., Jourdain, N. C., and Barnier, B.: Sea ice inertial oscillations in the Arctic Basin, The Cryosphere, 6, 1187–1201, 2012.

Haller, M., Brümmer, B., and Müller, G.: Atmosphere–ice forcing in the transpolar drift stream: results from the DAMOCLES ice-buoy campaigns 2007–2009, the Cryosphere, 8, 275–288, 2014.

Heil, P., and Hibler III, W. D.: Modeling the high-frequency component of Arctic sea ice drift and deformation, J. Phys. Oceanogr., 32, 3039–3057, 2002.

Held, A., Brooks, I. M., Leck, C., and Tjernström M.: On the potential contribution of open lead particle emissions to the central Arctic aerosol concentration, Atmos. Chem. Phys., 11, 3093–3105, https://doi.org/10.5194/acp-11-3093-2011, 2011.

Herman, A., and Glowacki, O.: Variability of sea ice deformation rates in the Arctic and their relationship with basin-scale wind forcing, The Cryosphere, 6(6), 1553–1559, doi:10.5194/tc-6-1553-2012, 2012.

Hutchings, J. K., and Hibler III, W. D.: Small-scale sea ice deformation in the Beaufort Sea seasonal ice zone, J. Geophys. Res., 113, C08032, doi:10.1029/2006JC003971, 2008.

Hutchings, J. K., Heil, P., Steer, A., and Hibler III, W. D.: Subsynoptic scale spatial variability of sea ice deformation in the western Weddell Sea during early summer, J. Geophys. Res., 117, C01002, doi:10.1029/2011JC006961, 2012.

Hutchings, J. K., Roberts, A., Geiger, C. A., and Richter-Menge, J.: Spatial and temporal characterization of sea-ice deformation, Ann. Glaciol., 52(57), 360–368, 2011.

Hutchings, J. K., Roberts, A., Geiger, C. A., and Richter-Menge, J.: Corrigendum: Spatial and temporal characterization of sea-ice deformation, J. Glaciol., 64(244), 343–346, 2018.

Hutter, N., Losch, M., and Menemenlis, D.: Scaling properties of arctic sea ice deformation in a high-resolution viscous-plastic sea ice model and in satellite observations, J. Geophys. Res. Oceans, 123, 672–687, https://doi.org/10.1002/2017JC013119, 2018.

Hutter, N., and Losch, M.: Feature-based comparison of sea ice deformation in lead-permitting sea ice simulations, The Cryosphere, 14, 93–113, https://doi.org/10.5194/tc-14-93-2020, 2020.

Itkin, P., Spreen, G., Cheng, B., Doble, M., Girard-Ardhuin, F., Haapala, J., Hughes, N., Kaleschke, L., Nicolaus, M., and Wilkinson, J.: Thin ice and storms: Sea ice deformation from buoy arrays deployed during N-ICE2015, J. Geophys. Res., 122, 4661–4674, doi:10.1002/2016JC012403, 2017.

Itkin, P., Spreen, G., Hvidegaard, S. M., Skourup, H., Wilkinson, J., Gerland, S., and Granskog, M. A.: Contribution of deformation to sea ice mass balance: A case study from an N-ICE2015 storm, Geophys. Res. Lett., 45, 789–796, https://doi.org/10.1002/2017GL076056, 2018.

Krumpen, T., Birrien, F., Kauker, F., and other coauthors: The MOSAiC ice floe: sediment-laden survivor from the Siberian shelf, The Cryosphere, 14, 2173–2187, https://doi.org/10.5194/tc-14-2173-2020, 2020.

Kwok, R.: Contrasts in sea ice deformation and production in the Arctic seasonal and perennial ice zones, J. Geophys. Res., 111, C11S22, doi:10.1029/2005JC003246, 2006.

Kwok, R., and Cunningham, G. F.: ICESat over Arctic sea ice: Estimation of snow depth and ice thickness, J. Geophys. Res., 113, C08010, doi:10.1029/2008JC004753, 2008.

Lammert, A., Brümmer, B., and Kaleschke, L.: Observation of cyclone-induced inertial sea-ice oscillation in Fram Strait, Geophys. Res. Lett., 36, L10503, doi:10.1029/ 2009GL037197, 2009.

Lei, R., Tian-Kunze, X., Leppäranta, M., Wang, J., Kaleschke, L., and Zhang Z.: Changes in summer sea ice, albedo, and portioning of surface solar radiation in the Pacific sector of Arctic Ocean during 1982–2009, J. Geophys. Res. Oceans, 121, 5470–5486, doi:10.1002/2016JC011831, 2016.

Lei, R., Gui, D., Hutchings, J. K., Wang, J., Pang X.: Backward and forward drift trajectories of sea ice in the northwestern Arctic Ocean in response to changing atmospheric circulation. Int. J. Climatol., 1–20. DOI: 10.1002/joc.6080, 2019.

Lei, R., Gui, D., Hutchings, J. K., Heil, P., Li, N.: Annual cycles of sea ice motion and deformation derived from buoy measurements in the western Arctic Ocean over two ice seasons. J. Geophys. Res., 125, e2019JC015310, https://doi.org/10.1029/2019JC015310, 2020a.

Lei, R., Gui, D., Heil, P., Hutchings, J.K., Ding, M.: Comparisons of sea ice motion and deformation, and their responses to ice conditions and cyclonic activity in the western Arctic Ocean between two summers, Cold Reg. Sci. Technol., 170, 102925, https://doi.org/10.1016/j.coldregions.2019.102925, 2020b.

Lewis, J. K., and Richter-Menge, J. A.: Motion-induced stresses in pack ice, J. Geophys. Res., 103(C10), 21831– 21843, doi:10.1029/98JC01262, 1998.

Lindell, D. B., and Long, D. G.: Multiyear Arctic ice classification using ASCAT and SSMIS. Remote Sens., 8, 294; doi:10.3390/rs8040294, 2016.

~~Lüpkes, C., Vihma, T., Birnbaum, G., and Wacker, U.: Influence of leads in sea ice on the temperature of the atmospheric boundary layer during polar night, Geophys. Res. Lett., 35, L03805, https://doi.org/10.1029/2007GL032461, 2008.~~

Lukovich, J. V., Babb, D. G., and Barber D. G.: On the scaling laws derived from ice beacon trajectories in the southern Beaufort Sea during the International Polar Year-Circumpolar Flaw Lead study, 2007–2008, J. Geophys. Res., 116, C00G07, doi:10.1029/2011JC007049, 2011.

Marsan, D., Stern, H., Lindsay, R., and Weiss, J.: Scale dependence and localization of the deformation of Arctic sea ice, Phys. Res. Lett., 93, 17, 178501, doi:10.1103/PhysRevLett.93.178501, 2004.

Marsan, D., and Weiss, J.: Space/time coupling in brittle deformation at geophysical scales, Earth Planet Sci. Lett., 296(3–4), 353–359, 2010.

Moore, G. W. K., Schweiger, A., Zhang, J., and Steele, M.: Collapse of the 2017 winter Beaufort High: A response to thinning sea ice? Geophys. Res. Lett., 45: 2860–2869. https://doi.org/10.1002/2017GL076446, 2018.

Nicolaus, M., Katlein, C., Maslanik, J., and Hendricks, S.: Changes in Arctic sea ice result in increasing light transmittance and absorption, Geophys. Res. Lett., 39, L24501, doi:10.1029/2012GL053738, 2012

Oikkonen, A., Haapala, J., Lensu, M., Karvonen, J., and Itkin, P.: Small-scale sea ice deformation during N-ICE2015: From compact pack ice to marginal ice zone, J. Geophys. Res. Oceans, 122, 5105–5120, doi:10.1002/2016JC012387, 2017.

Perovich, D. K., Grenfell, T. C., Richter-Menge, J. A., Light, B., Tucker III, W. B., and Eicken, H.: Thin and thinner: sea ice mass balance measurements during SHEBA, J. Geophys. Res., 108(C3), 8050, doi:10.1029/2001JC001079, 2003.

Perovich, D., Meier, W., Tschudi, M., Farrell, S, Hendricks, S., Gerland, S., Kaleschke, L., Ricker, R., Tian-Kunze, X., Webster, M., and Wood, K.: Sea ice. Arctic report card 2019, 26–34, http://www.arctic.noaa.gov/Report-Card, 2019.

Perovich, D. K., and Polashenski, C.: Albedo evolution of seasonal Arctic sea ice, Geophys. Res. Lett., 39, L08501, doi:10.1029/2012GL051432, 2012.

Proshutinsky, A., Krishfield, R., Timmermans, M. L., Toole, J., Carmack, E., McLaughlin, F., Williams, W. J., Zimmermann, S., Itoh, M., and Shimada, K.: Beaufort Gyre freshwater reservoir: State and variability from observations. J. Geophys. Res., 114, C00A10, doi:10.1029/2008JC005104, 2009.

Rampal, P., Weiss, J., Marsan, D., Lindsay, R., and Stern, H.: Scaling properties of sea ice deformation from buoy dispersion analysis. J. Geophys. Res., 113, C03002, doi:10.1029/2007JC004143, 2008.

Rampal, P., Dansereau, V., Olason, E., Bouillon, S., Williams, T., Korosov, A., and Samaké, A.: On the multi-fractal scaling properties of sea ice deformation Article, Cryosphere, 13(9), 2457–2474, 2019.

Salganik, E., Høyland, K. V., and Maus, S.: Consolidation of fresh ice ridges for different scales. Cold Reg. Sci. Technol., 171, 102959, https://doi.org/10.1016/j.coldregions.2019.102959, 2020.

Screen, J. A., Simmonds, I.: Increasing fall-winter energy loss from the Arctic Ocean and its role in Arctic temperature amplification, Geophys. Res. Lett., 37, L16707, doi:10.1029/2010GL044136, 2010.

Serreze, M. C., and Meier, W. N.: The Arctic's sea ice cover: trends, variability, predictability, and comparisons to the Antarctic. Ann. N. Y. Acad. Sci., doi:10.1111/nyas.13856, 2018.

Spreen, G., Kwok, R., and Menemenlis, D.: Trends in Arctic sea ice drift and role of wind forcing: 1992–2009, Geophys. Res. Lett., 38: L19501, doi: 10.1029/2011GL048970, 2011.

Spreen, G., Kaleschke, L., and Heygster, G.: Sea ice remote sensing using AMSR-E 89 GHz channels J. Geophys. Res.,vol. 113, C02S03, doi:10.1029/2005JC003384, 2008.

Spreen, G., Kwok, R., Menemenlis, D., and Nguyen, A. T.: Sea-ice deformation in a coupled ocean–sea-ice model and in satellite remote sensing data, The Cryosphere, 11, 1553–1573, https://doi.org/10.5194/tc-11-1553-2017, 2017.

Steele, M., and Dickinson, S.: The phenology of Arctic Ocean surface warming, J. Geophys. Res. Oceans, 121, 6847–6861, doi:10.1002/2016JC012089, 2016.

Stern, H. L., and Lindsay, R. W.: Spatial scaling of Arctic sea ice deformation, J. Geophys. Res., 114, C10017, doi:10.1029/2009JC005380, 2009.

Stern H. L., and Moritz, R. E.: Sea ice kinematics and surface properties from RADARSAT synthetic aperture radar during the SHEBA drift, J. Geophys. Res., 107(C10), 8028, doi:10.1029/2000JC000472, 2002.

Strong, C., and Rigor, I. G.: Arctic marginal ice zone trending wider in summer and narrower in winter, Geophys. Res. Lett., 40, 4864–4868, doi:10.1002/grl.50928, 2013.

Tschudi, M., Meier, W. N., Stewart, J. S., Fowler, C., and Maslanik, J.: Polar Pathfinder Daily 25 km EASE-Grid Sea Ice Motion Vectors, Version 4, Boulder, CA, USA, NASA National Snow and Ice Data Center Distributed Active Archive Center, https://doi.org/10.5067/INAWUWO7QH7B, 2019

Tschudi, M. A., Meier, W. N., and Stewart, J. S.: An enhancement to sea ice motion and age products at the National Snow and Ice Data Center (NSIDC), the Cryosphere, 14(5), 1519-1536, 2020.

Vihma, T., Tisler, P., Uotila, P.: Atmospheric forcing on the drift of Arctic sea ice in 1989–2009, Geophys. Res. Lett. 39: L02501, doi: http://dx.doi.org/10.1029/2011GL050118, 2012.

Wang, J., Zhang, J., Watanabe, E., Mizobata, K., Ikeda, M., Walsh, J. E., Bai, X., Wu, B.: Is the Dipole Anomaly a major driver to record lows in the Arctic sea ice extent? Geophys. Res. Lett. 36: L05706. doi:10.1029/2008GL036706, 2009.

Woodgate, R. A., Weingartner, T. J., and Lindsay, R.: Observed increases in Bering Strait oceanic fluxes from the Pacific to the Arctic from 2001 to 2011 and their impacts on the Arctic Ocean water column. Geophys. Res. Lett., 39, L24603, doi:10.1029/2012GL054092, 2012.

Zhang, Y., Maslowski, W., and Semtner, A. J.: Impact of mesoscale ocean currents on sea ice in high-resolution Arctic ice and ocean simulations, J. Geophys. Res., 104(C8),18409–18429, doi:10.1029/1999JC900158, 1999.

Zhao, M., Timmermans, M.-L., Cole, S., Krishfield, R., and Toole, J.: Evolution of the eddy field in the Arctic Ocean's Canada Basin, 2005–2015, Geophys. Res. Lett., 43, 8106–8114, doi:10.1002/2016GL069671, 2016.

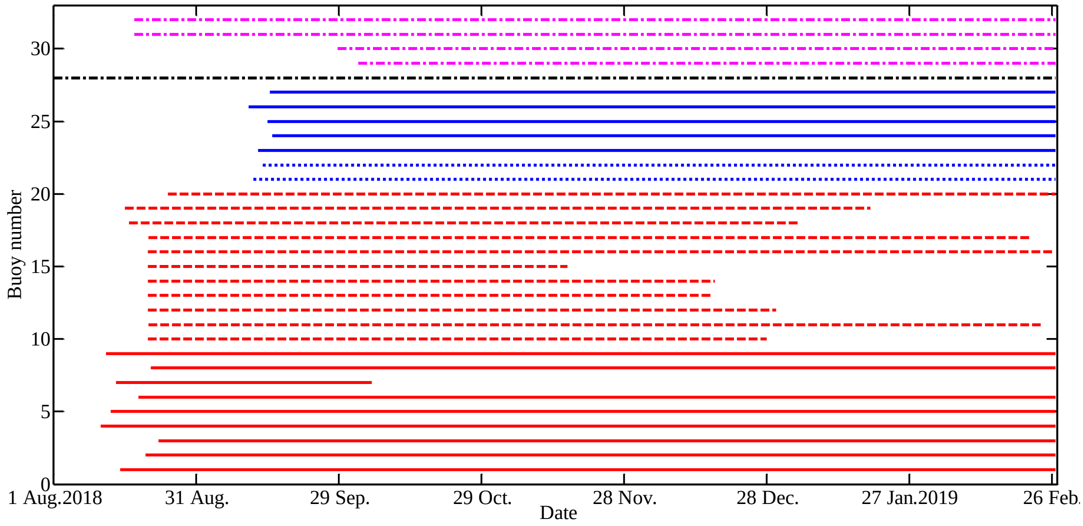

Figure 1 Operational periods of all buoys included in this study. Red lines denote buoys deployed during CHINARE in August 2018; blue lines denote buoys deployed during T-ICE; black line indicates the buoy deployed during CHINARE 2016; purple lines represent IABP buoys. Solid, dashed, short-dashed, and dot-dashed lines denote SIMBA, TUT, SB, and iSVP or other buoys, respectively.

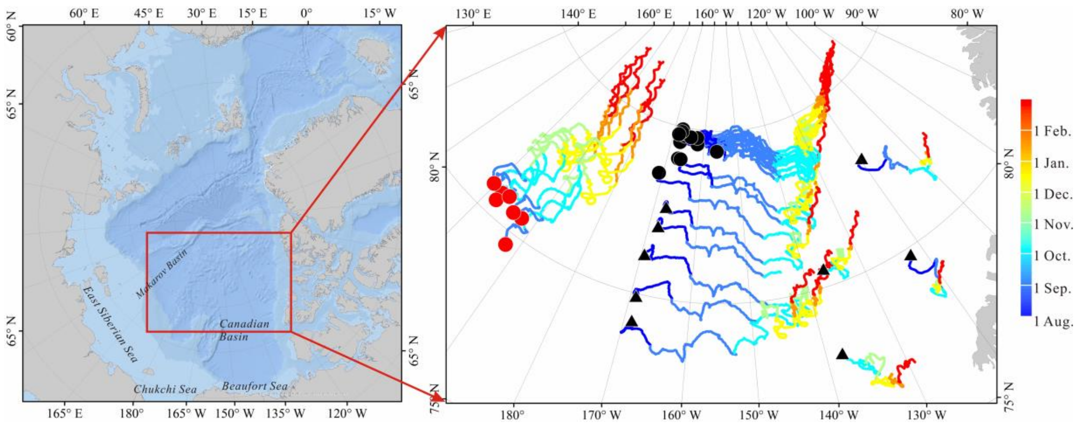

Figure 2 Buoy trajectories between deployment sites (indicated by circles and triangles) and buoy locations on 28 February 2019. Trajectories from 15 buoys deployed during CHINARE at locations indicated by black circles and 7 buoys deployed during T-ICE at locations indicated by red circles were used to estimate ice deformation rate. For buoys deployed prior to August 2018, the starting point of the trajectory was set to 1 August 2018.

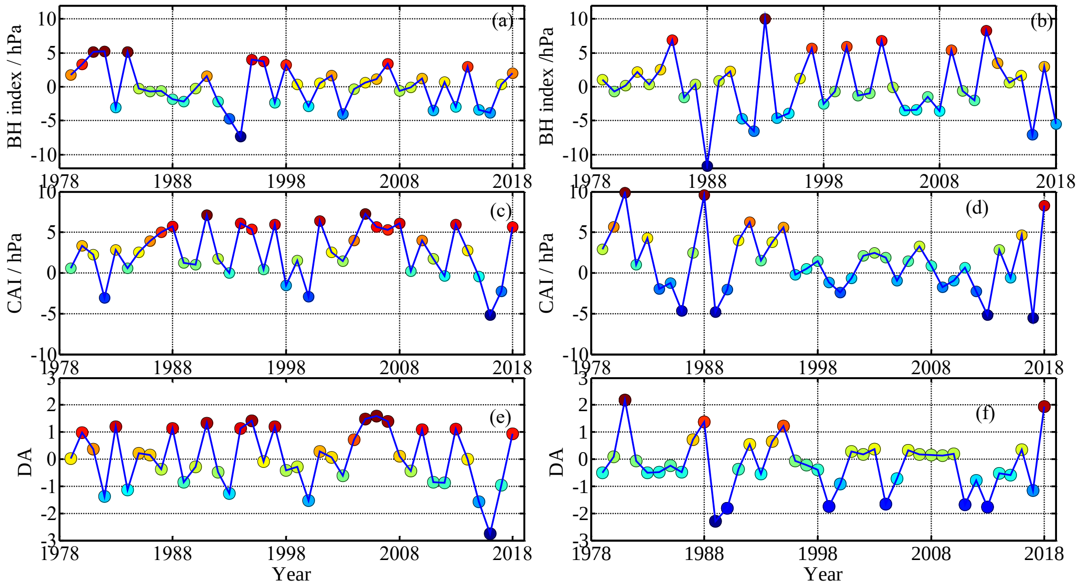

Figure 3 Changes in (a) autumn (SON) and (b) winter (DJF) BH index, (c) autumn and (d) winter CAI, and (e) autumn and (f) winter DA from 1979 to 2018.

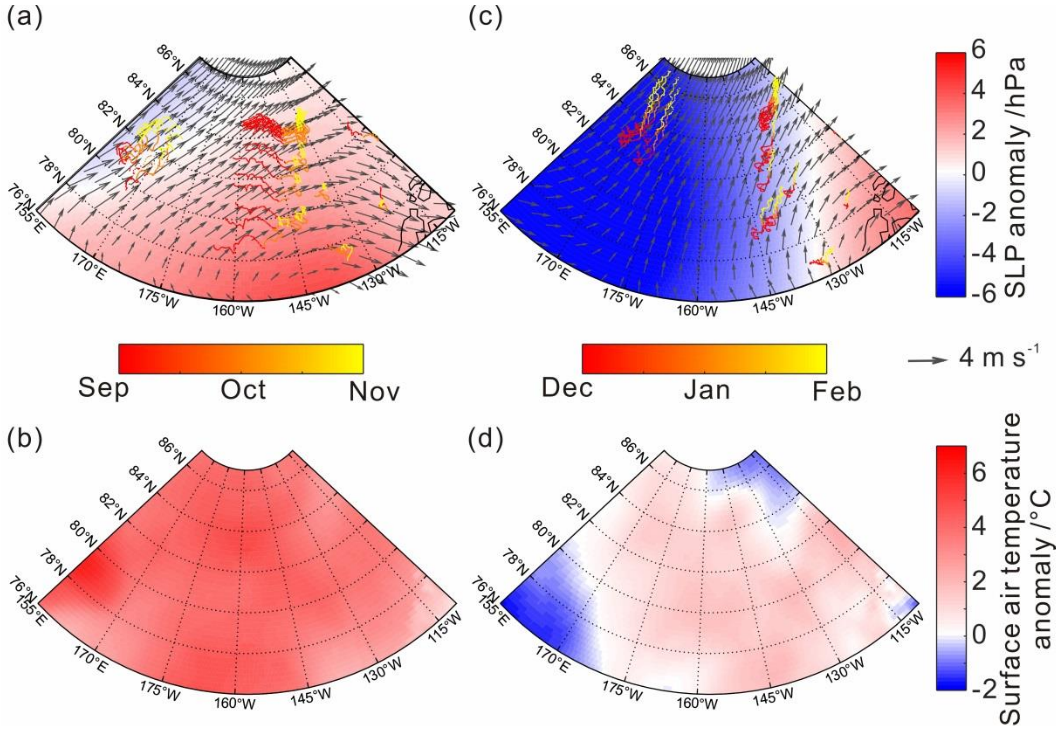

Figure 4 Anomalies of (a and c) SLP and (b and d) near-surface air temperature (2 m) over the PAO during (a and b) autumn 2018 and (c and d) winter 2018/19 relative to 1979–2018 climatology; (a and c) arrows indicate seasonal average wind vectors and colored lines indicate buoy trajectories through time.

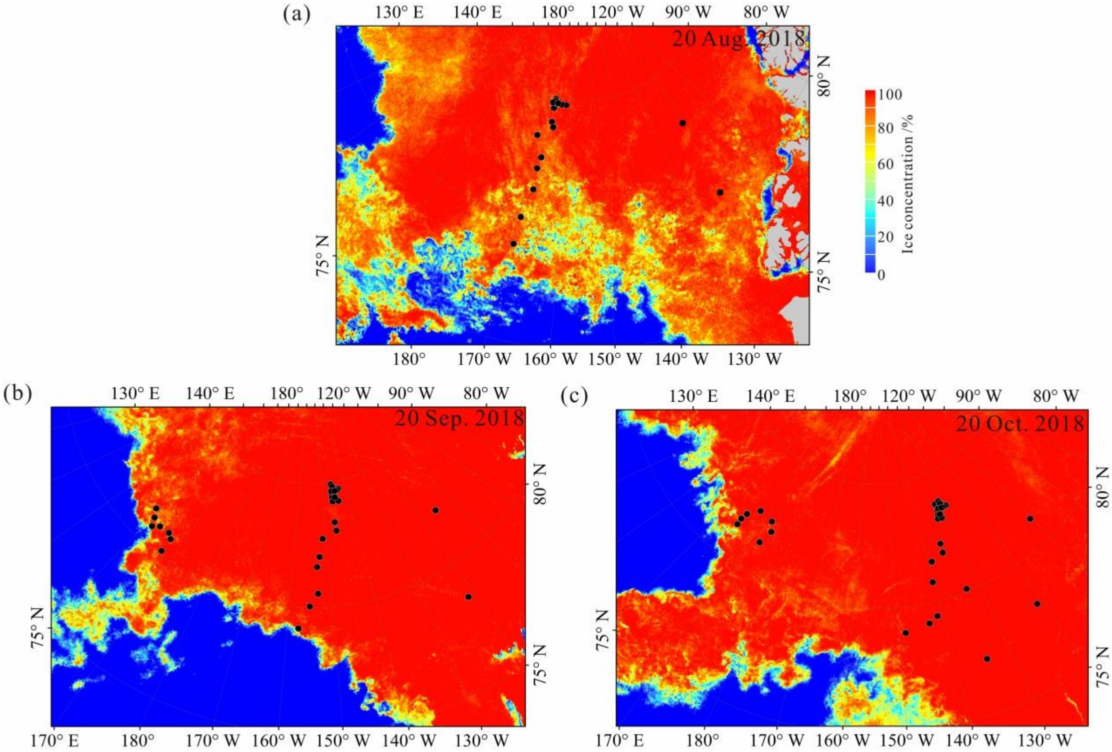

Figure 5 Sea ice concentration across the PAO on 20 of (a) August, (b) September, and (c) October, 2018, with black dots denoting buoy positions on the given days.

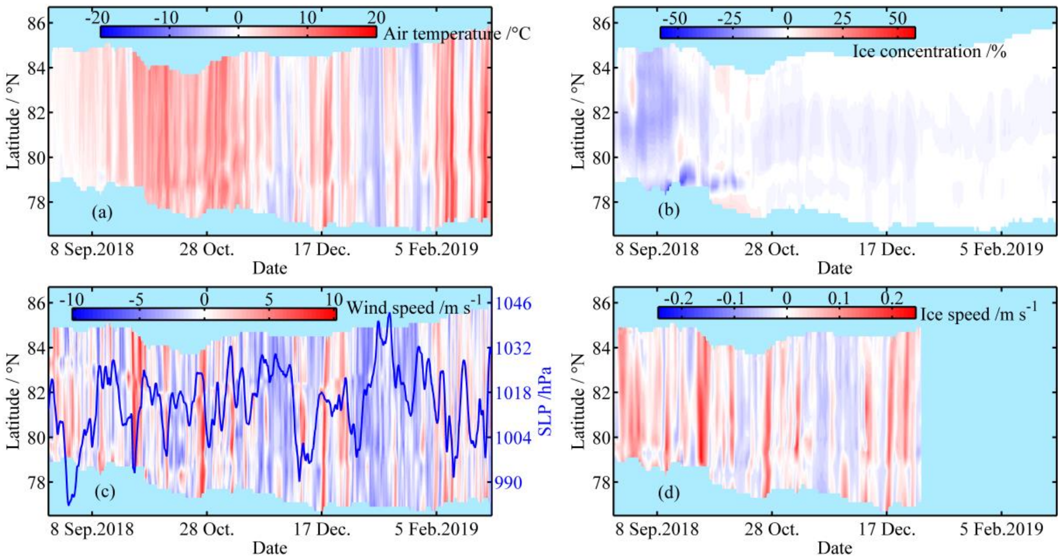

Figure 6 Meridional and temporal changes in anomalies of (a) T_{2m}, (b) ice concentration, (c) wind speed, (d) ice speed in the ice season 2018/19 relative to 1979–2018 climatology; (c) blue line indicates SLP averaged over the study region.

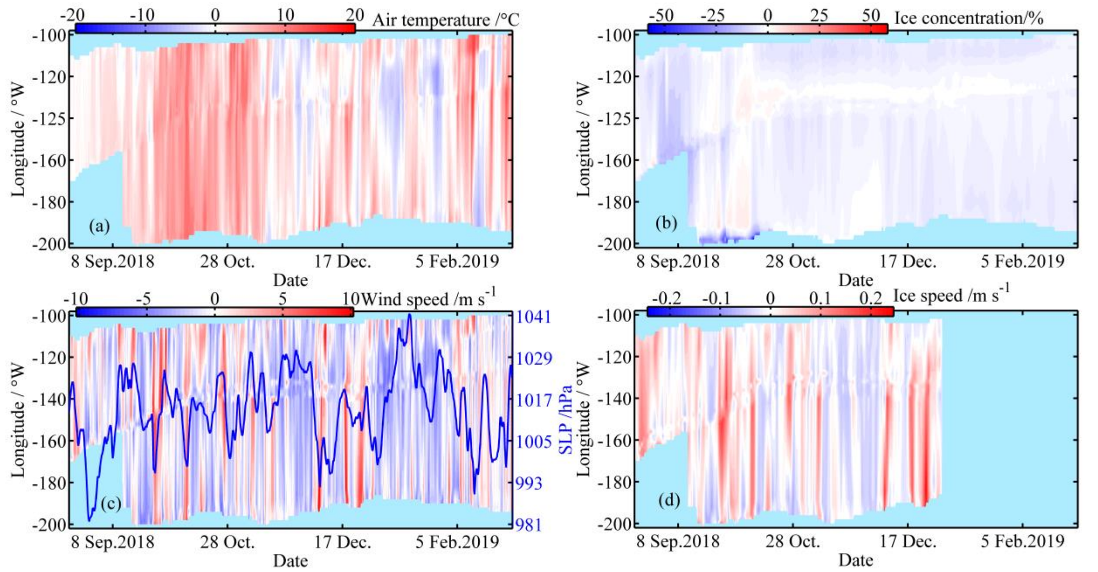

Figure 7 Same as Fig 2, but for zonal changes. Longitudes with values below −180 denote the eastern Arctic.

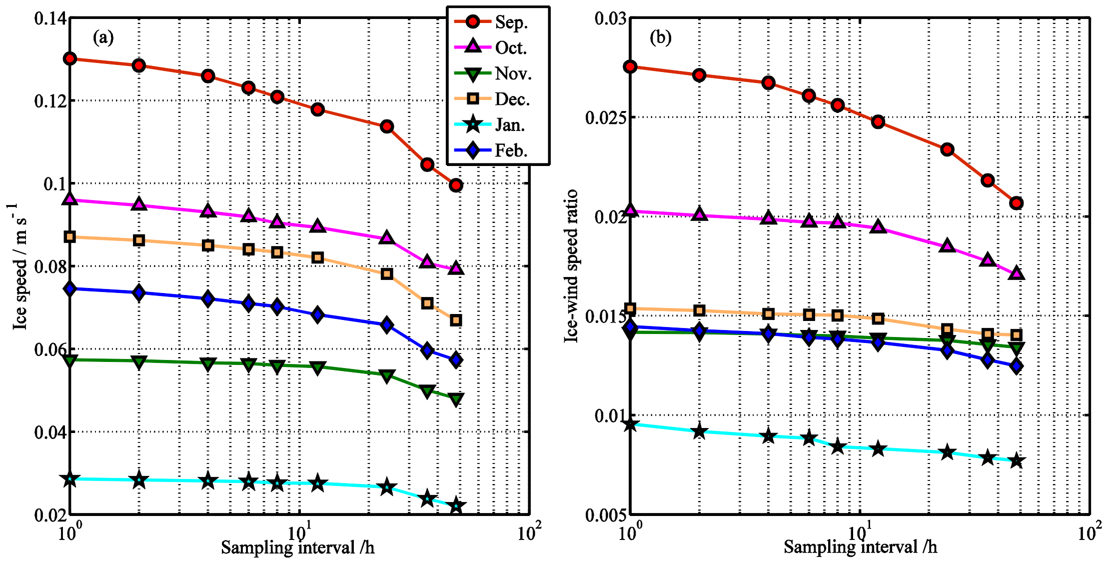

Figure 8 Changes in (a) ice speed and (b) IWSR as a function of position data resampling interval for various months in 2018/19.

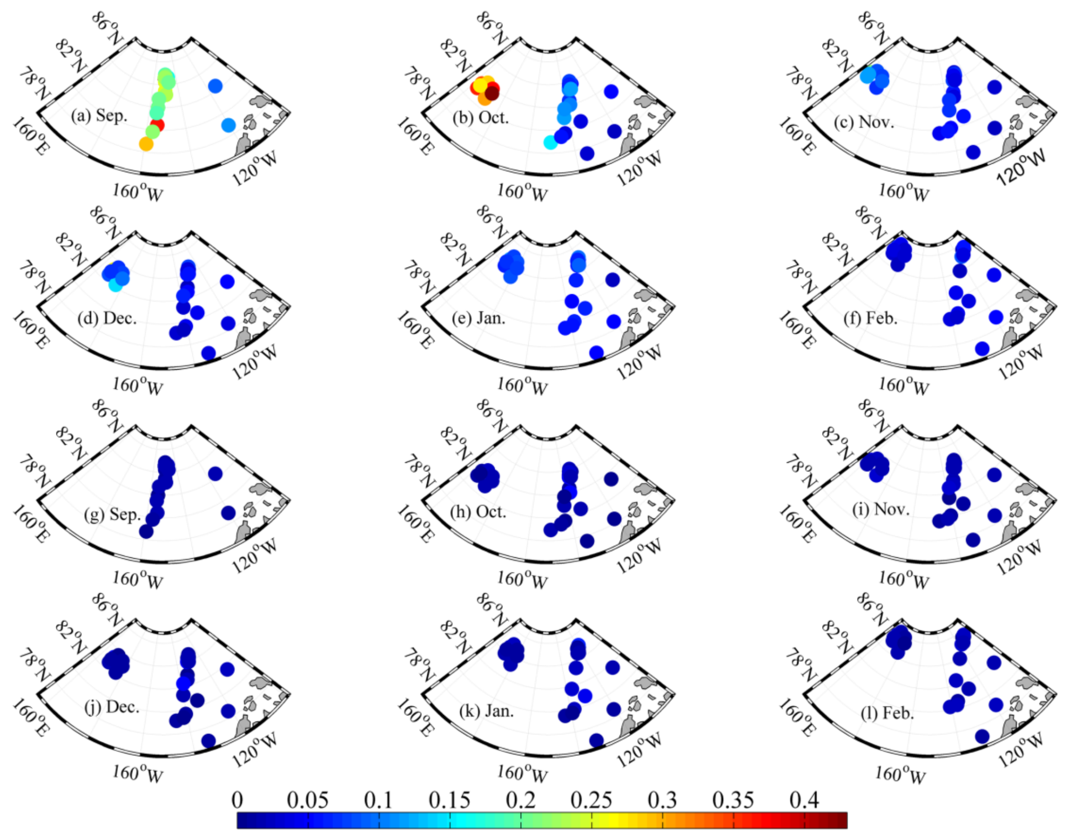

Figure 9 Amplitudes after Fourier transformation of monthly time series of normalized ice velocity at the negative-phase inertial frequency (a–f) and positive-phase semidiurnal frequency (g–l) from September 2018 to February 2019.

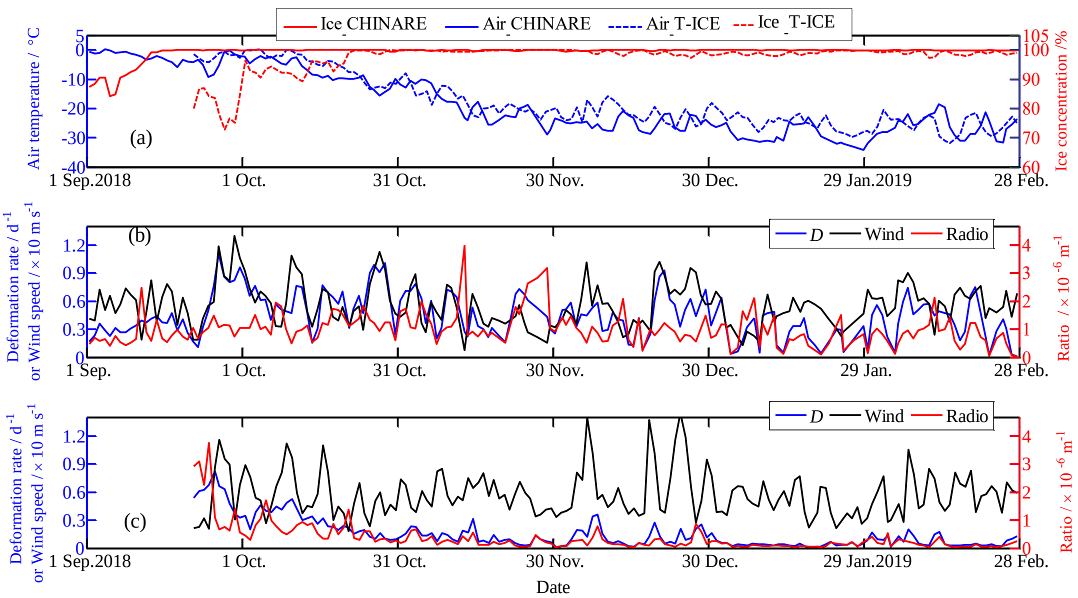

Figure 10 (a) Time series of daily average near-surface (2 m) air temperature and ice concentration within the CHINARE and T-ICE buoy clusters. Ice deformation rate (*D*), wind speed and their ratio at the 10–20 km scale for the (b) CHINARE and (c) T-ICE buoy clusters.

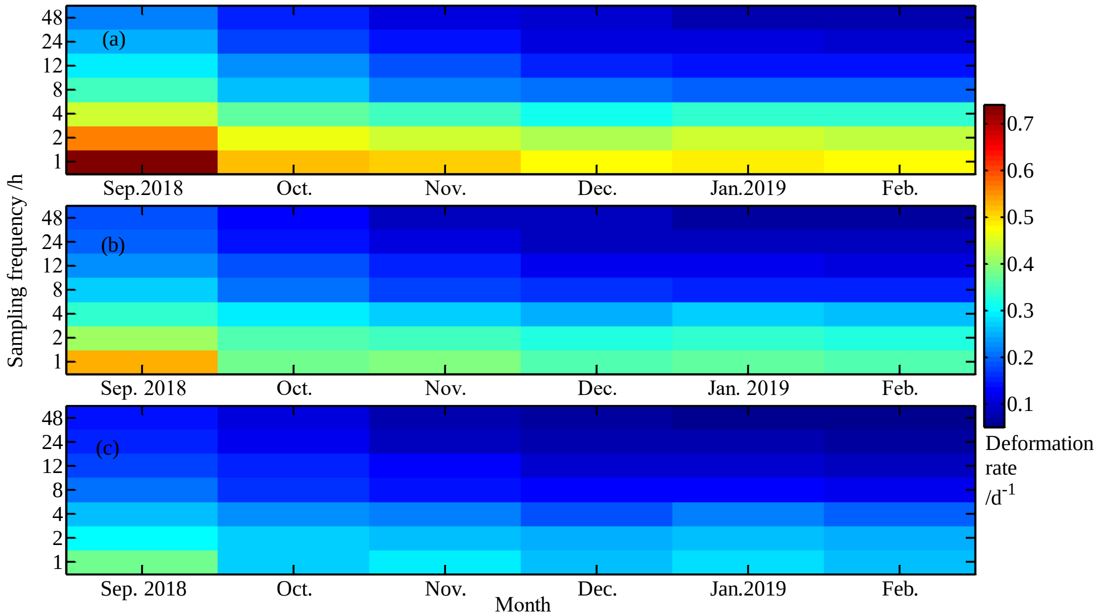

Figure 11 Monthly average sea ice deformation rate calculated from the CHINARE buoy cluster at length scales of (a) 7.5 km, (b) 15 km, and (c) 30 km using position data resampled at various intervals between 1 and 48 h.

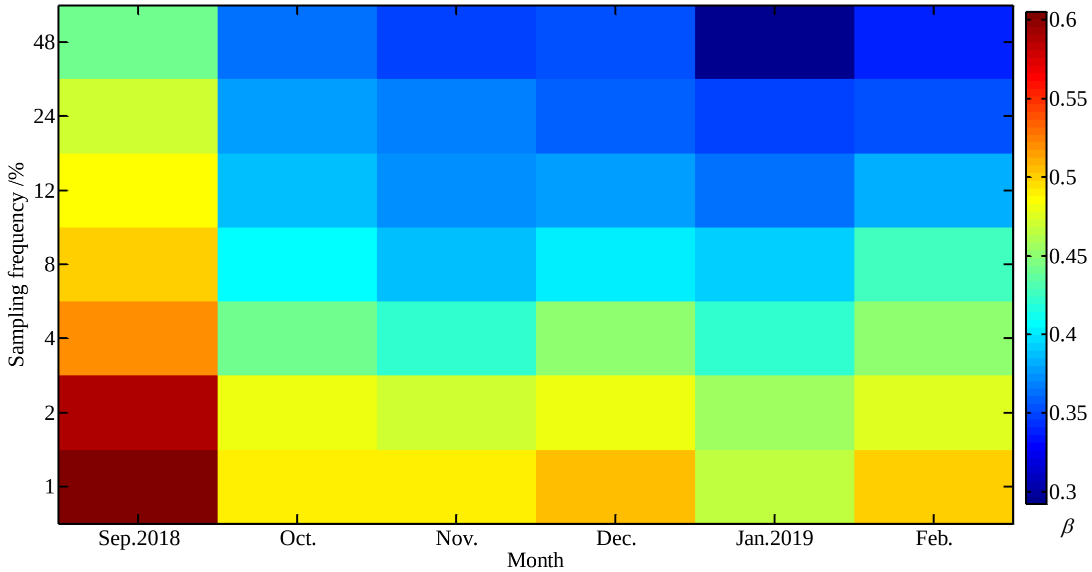

Figure 12 Changes in monthly spatial scaling exponent as a function of position data resampling frequency obtained from the CHINARE buoy cluster.

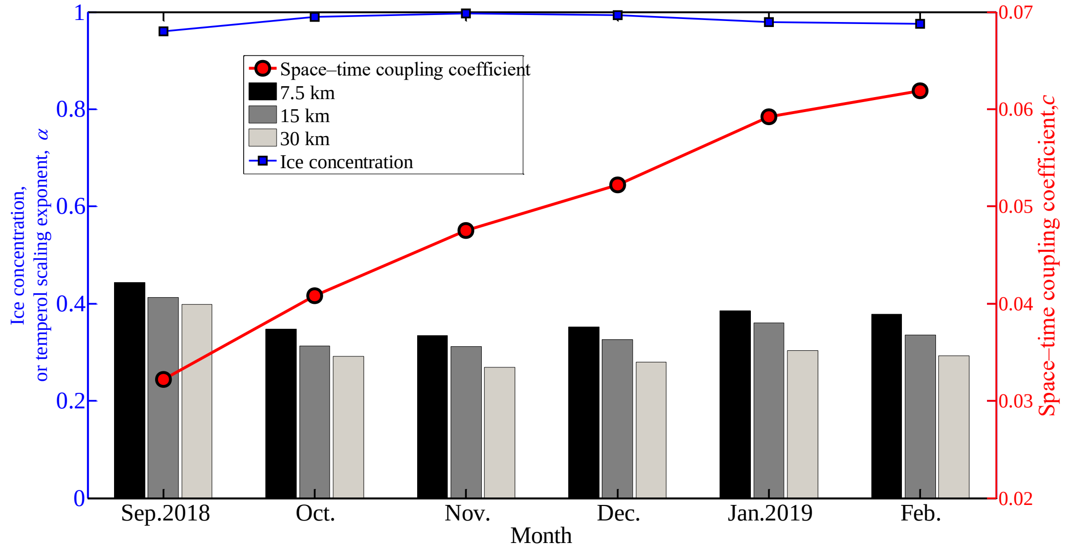

Figure 13 Changes in monthly temporal scaling exponent at various length scales, space–time coupling coefficient, and average ice concentration within the CHINARE buoy cluster.

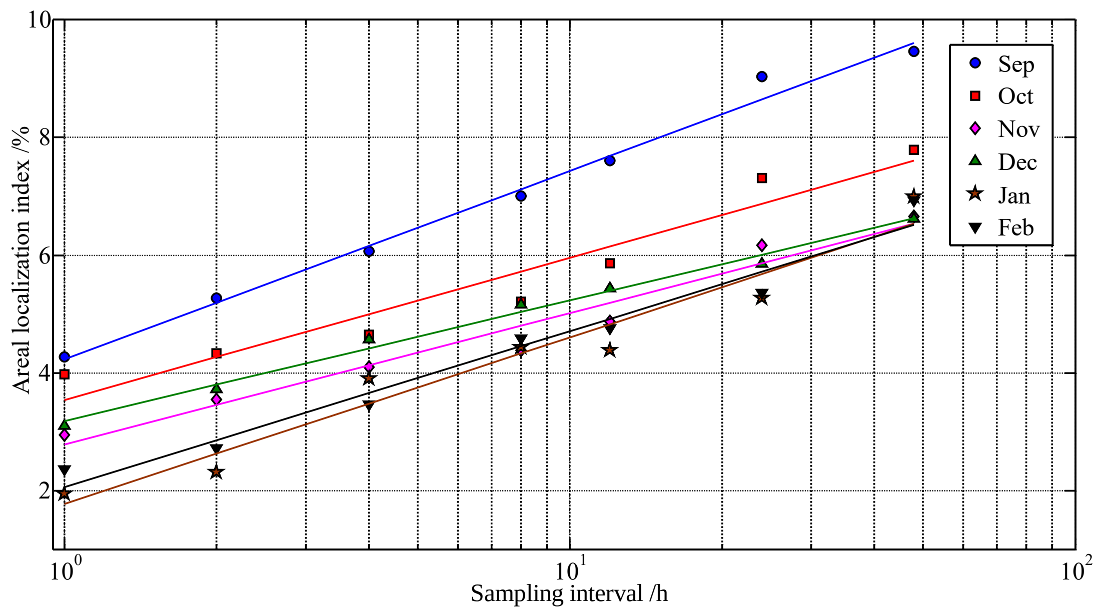

Figure 14 Changes in monthly (September 2018 to February 2019) areal localization index of ice deformation at a scale of 10–20 km as a function of the position data resampling frequency.

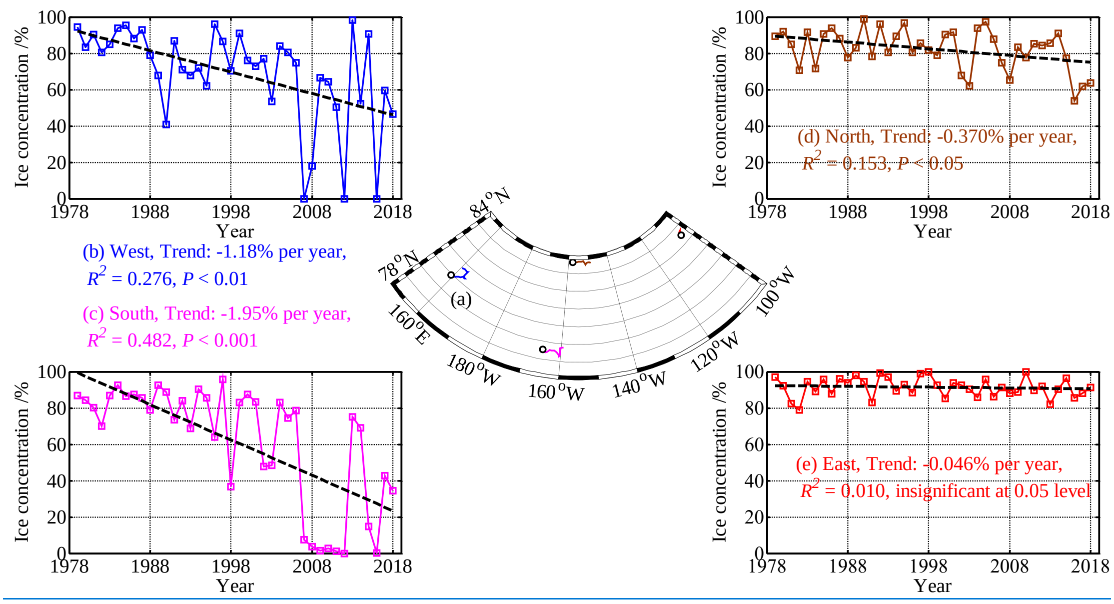

Figure 15 (a) Drift trajectories of the westernmost, southernmost, near northernmost, and easternmost buoys from 1 to 15 September 2018; the northernmost buoy has been omitted because it drifted to the north of 84.5° N, where SMMR ice concentration data prior to 1987 are unavailable; trajectory of the westernmost buoy was reconstructed using the NSIDC ice motion product because this buoy was deployed on 15 September 2018; (b–e) Long-term changes in ice concentration along buoy trajectories averaged over 1–15 September, with black lines denoting linear trends.

Table 1. Statistical relationships between IWSR and selected parameters. Significance levels are *P* < 0.001 (***), *P* < 0.01 (**), and *P* < 0.05 (*), and n.s. denotes insignificant at the 0.05 confidence level. Numbers in parentheses indicate number of buoys used for the statistics.

Month	vs. Lat.	vs. Lon.	vs. W_{10m}	vs. T_{2m}
20 Aug.-30 Sep.	–0.647**(24)	–0.738***(29)	–0.542**(32)	n.s.
Oct.	–0.811***(24)	–0.885***(29)	–0.866***(32)	0.657***(32)
Nov.	–0.777***(23)	–0.765***(28)	n.s.	0.736***(32)
Dec.	–0.736***(22)	–0.829***(27)	n.s.	0.675***(32)
Jan.	n.s.	–0.711**(23)	n.s.	n.s.
Feb.	n.s.	–0.610**(23)	n.s.	n.s.